1991ApJ...377..559R

THE ASTROPHYSICAL JOURNAL, 377:559–580, 1991 August 20

COLLISIONS OF GIANT STARS WITH COMPACT OBJECTS: HYDRODYNAMICAL CALCULATIONS

FREDERIC A. RASIO[1] AND STUART L. SHAPIRO[1,2]
Center for Radiophysics and Space Research, Space Sciences Building, Cornell University, Ithaca, NY 14853
Received 1990 November 26; accepted 1991 February 25

ABSTRACT

Encounters between a $0.8M_\odot$ giant star and a $1.4M_\odot$ compact object on a parabolic orbit have been calculated using smooth particle hydrodynamics (SPH). Both the stellar core and the compact object are represented by point masses interacting with the gas through gravity only. We find that all encounters with periastron distance $r_p \lesssim 2.5R_G$, where R_G is the stellar radius, lead to significant disruption of the stellar envelope, including some mass loss. When $r_p/R_G \lesssim 0.5$, the envelope is completely destroyed during the collision. About 40% of the gas escapes, while the rest forms a massive disk around the compact object, leaving behind the bare stellar core on a highly eccentric orbit. Subsequent close passages lead to continuous extraction of gas from the disk at a large rate, and the binary orbit may eventually stabilize while still retaining a large eccentricity. For $0.5 \lesssim r_p/R_G \lesssim 2.5$, complete destruction of the envelope is avoided during the first close passage. However, nonlinear effects tend to make the envelope expand by a large factor, so that subsequent close passages will likely destroy it. In particular, we confirm Bailyn's prediction that all captures of a neutron star by a red giant in globular clusters are likely to result in the eventual destruction of the red giant envelope. We discuss the implications of our results in light of recent new detections of millisecond pulsars in globular clusters. Most importantly, we suggest that many globular cluster pulsars may have been spun-up by accretion from a massive disk rather than from a binary companion, thereby providing a possible solution to the birthrate problem.

To support our findings, we present various new tests of our SPH treatment. In particular, we calculate tidal encounters between a polytrope and a point mass and find good agreement with semianalytic, linear perturbation calculations. Both head-on and off-axis collisions between a polytrope and a point mass are also examined, and our SPH results are compared to those of recent finite-difference calculations.

Subject headings: hydrodynamics — pulsars — stars: binaries — stars: evolution — stars: stellar dynamics — X-rays: binaries

1. INTRODUCTION

The recent discoveries of several binary pulsars in globular clusters (Lyne et al. 1988; Anderson et al. 1989; Wolszczan et al. 1989; Anderson et al. 1990a, b; D'Amico et al. 1990; Lyne et al. 1990; Lyne 1991) suggest that it may be time to reexamine in detail the possible formation mechanisms of these sources. Two basic mechanisms have been proposed. One invokes a tidally dissipative, two-body encounter between a compact object and an ordinary main-sequence or giant star (Fabian, Pringle, & Rees 1975). The other, proposed by Sutantyo (1975), assumes that a direct physical collision takes place between a giant star and a compact object. Recently, Verbunt (1987) and Verbunt & Meylan (1988) used globular cluster data to calculate relative formation rates through various mechanisms and concluded that collisions with red giant or horizontal-branch stars provide the most efficient way of forming binary systems containing a neutron star and a white dwarf. Many detailed calculations of the Fabian, Pringle, & Rees mechanism have been performed (Press & Teukolsky 1977; Lee & Ostriker 1986; Giersz 1986; McMillan, McDermott, & Taam 1987; Ray, Kembhavi, & Antia 1987; McMillan, Taam, & McDermott 1990). These calculations are all based on linear perturbation expansions in terms of the normal modes of oscillation of the star. However, few general calculations of collisions with a giant star have been attempted (see Tuchman 1985; Livne & Tuchman 1988), and all of them were very approximate. This is because of the highly nonlinear nature of the interaction and the difficulty of doing numerical hydrodynamics in three dimensions.

In a previous paper (Rasio & Shapiro 1990, hereafter Paper I), we used simple N-body simulations to study the dynamics of collisions between a point mass and a giant star. The star was modeled as a point mass core surrounded by an envelope made of N individual particles interacting through gravity only. Since we used relatively small numbers of particles ($N \sim 500$), it was possible to explore rather systematically the entire parameter space of the problem. However, the detailed hydrodynamics of the interaction could not be treated correctly. Our approach in Paper I was very general. In particular, the mass ratio, impact parameter, and relative velocity at infinity were all allowed to vary independently and over a wide range of values. For globular clusters, however, a more restricted approach is adequate. The small stellar velocity dispersions imply that the initial orbit for any two-body encounter is quasi-parabolic. Moreover, the mass of giant stars is known to be $\approx 0.8\ M_\odot$, from the position of the main-sequence turnoff point. In this paper, we will therefore only consider parabolic encounters between a $0.8\ M_\odot$ giant and a $1.4\ M_\odot$ neutron star. Here our

---

[1] Department of Physics, Cornell University.

[2] Department of Astronomy, Cornell University.

discussion will be based on *three-dimensional hydrodynamical calculations* of such encounters, which we performed using smooth particle hydrodynamics (SPH).

Our paper is organized as follows. In § 2 we describe our implementation of SPH and present the results of several test-bed calculations. In particular, we simulate tidal encounters with a polytrope and compare our numerical results to those obtained by semi-analytic methods. In § 3, we summarize calculations of *collisions* between a point mass and a polytrope. These calculations provide a first step towards the more realistic treatment of § 4, while still allowing comparisons with previous finite-difference calculations. In § 4, we construct a simple hydrodynamical model for a giant star and use this model to calculate parabolic encounters with a neutron star. Finally, in § 5, we discuss the astrophysical implications of our results.

2. METHOD AND TEST CALCULATIONS

In Paper I we used a simple N-body method to simulate the dynamics of a giant star's envelope via a small number ($N \approx 500$) of point masses interacting only through gravitational forces. This idealization had the advantage of simplicity, allowing us to perform a large number of fully three-dimensional calculations spanning a large parameter space. Here, instead, we seek higher accuracy at the expense of generality. The SPH method provides a natural way of achieving this goal, essentially by adding a new pressure gradient term to the equations of motion of the particles. It allows us to calculate with reasonable accuracy the dynamical effects of fluid phenomena such as shocks and rarefaction waves while still retaining a three-dimensional description. The much higher computational cost of the method, however, implies that we have to focus on a considerably smaller subset of values for the parameters of the problem. Namely, for a given stellar model, only parabolic encounters will be considered. High-velocity encounters, considered in Paper I, will not be discussed here. Moreover, we are able to perform full-scale calculations for only a small number of representative cases.

2.1. *Smooth Particle Hydrodynamics*

Smooth particle hydrodynamics, introduced some time ago (Gingold & Monaghan 1977; Lucy 1977), has since been refined considerably and used to study a wide variety of astrophysical problems including galaxy formation (Shapiro, Kang, & Villumsen 1989), supernovae (Nagasawa, & Miyama 1988), tidal disruption by a massive black hole (Evans & Kochanek 1989), and interstellar cloud collisions (Lattanzio et al. 1985), as well as stellar collisions (Benz & Hills 1987; Benz, Hills, & Thielemann 1989). Many different implementations of SPH have been employed (Evrard 1988; Hernquist & Katz 1989; Monaghan & Lattanzio 1985). Here we give only a brief description of our own implementation, referring the reader to the review article by Monaghan (1985) for a more general discussion.

As in the case of N-body simulations (Paper I), our code must solve the equations of motion of a large number N of particles,

$$\begin{aligned} \dot{\boldsymbol{r}}_i &= \boldsymbol{v}_i \,, \\ m_i \dot{\boldsymbol{v}}_i &= \boldsymbol{F}_i^{(\mathrm{Grav})} + \boldsymbol{F}_i^{(\mathrm{SPH})} \,. \end{aligned} \tag{1}$$

The SPH method allows us to calculate an effective pressure-gradient force acting on each individual particle. In addition to its position $\boldsymbol{r}_i$, velocity $\boldsymbol{v}_i$, and mass m_i, each particle carries two new, SPH–specific parameters: a physical parameter u_i, representing the internal energy per unit mass in the fluid at $\boldsymbol{r}_i$, and a purely numerical "smoothing length," h_i, specifying the local spatial resolution. An estimate of the fluid density at $\boldsymbol{r}_i$ is calculated from the masses, positions, and smoothing lengths of neighboring particles as a local weighted average,

$$\rho_i = \sum_j m_j W_{ij} \,. \tag{2}$$

Symmetric weights $W_{ij} = W_{ji}$ are calculated following the method of Hernquist & Katz (1989) as

$$W_{ij} = \tfrac{1}{2}[W(|\boldsymbol{r}_i - \boldsymbol{r}_j|, h_i) + W(|\boldsymbol{r}_i - \boldsymbol{r}_j|, h_j)] \,. \tag{3}$$

Here $W(r, h)$ is an interpolation kernel, for which we use the second-order accurate form of Monaghan & Lattanzio (1985),

$$W(r, h) = \frac{1}{\pi h^3} \begin{cases} 1 - \dfrac{3}{2}\left(\dfrac{r}{h}\right)^2 + \dfrac{3}{4}\left(\dfrac{r}{h}\right)^3 , & 0 \le \dfrac{r}{h} < 1 \,, \\ \dfrac{1}{4}\left[2 - \left(\dfrac{r}{h}\right)\right]^3 , & 1 \le \dfrac{r}{h} < 2 \,, \\ 0 \,, & \dfrac{r}{h} \ge 2 \,. \end{cases} \tag{4}$$

When the true density $\rho(\boldsymbol{r})$ of the fluid is presented by an appropriate distribution of particle positions, masses, and smoothing lengths, one can show that $\rho_i = \rho(\boldsymbol{r}_i) + O(h_i^2)$ (see, e.g., Monaghan 1985). Since our calculations assume an adiabatic equation of state for the gas, the pressure at $\boldsymbol{r}_i$ will be estimated as

$$p_i = (\gamma - 1)\rho_i u_i \,, \tag{5}$$

where γ is the constant ratio of specific heats. The local speed of sound is $c_i = (\gamma p_i/\rho_i)^{1/2}$.

The hydrodynamical part of the force on particle i is calculated as

$$\mathbf{F}_i^{(\mathrm{SPH})} = -\sum_j m_i m_j \left[\left(\frac{p_i}{\rho_i^2} + \frac{p_j}{\rho_j^2}\right) + \Pi_{ij}\right] \nabla_i W_{ij} . \tag{6}$$

Here Π_{ij} is an artificial viscosity term, while the rest of the above expression represents one of many possible SPH estimators for the local pressure gradient force $-(\nabla p/\rho)_i$ (see, e.g., Monaghan 1985). This form has the advantage of being computationally convenient, while at the same time providing a natural set of conservation laws as described below. For the artificial viscosity we adopt a symmetrized version of the form proposed by Monaghan (1989),

$$\Pi_{ij} = \frac{-\alpha \mu_{ij} c_{ij} + \beta \mu_{ij}^2}{\rho_{ij}} , \tag{7}$$

where $\rho_{ij} = (\rho_i + \rho_j)/2$, $c_{ij} = (c_i + c_j)/2$, and

$$\mu_{ij} = \begin{cases} \dfrac{(\mathbf{v}_i - \mathbf{v}_j) \cdot (\mathbf{r}_i - \mathbf{r}_j)}{h_{ij}(|\mathbf{r}_i - \mathbf{r}_j|^2/h_{ij}^2 + \eta^2)} , & \text{when } (\mathbf{v}_i - \mathbf{v}_j) \cdot (\mathbf{r}_i - \mathbf{r}_j) < 0 , \\ 0 , & \text{when } (\mathbf{v}_i - \mathbf{v}_j) \cdot (\mathbf{r}_i - \mathbf{r}_j) \geq 0 , \end{cases} \tag{8}$$

with $h_{ij} = (h_i + h_j)/2$. This represents a combination of the usual von Neuman–Richtmyer artificial viscosity and a bulk viscosity. It provides a good description of shocks when the constants satisfy $\alpha \approx \beta \approx 2$, and $\eta^2 \sim 10^{-2}$ (Monaghan 1989; Hernquist & Katz 1989).

To complete the description of the fluid, we write the first law of thermodynamics at $\mathbf{r}_i$ as

$$\frac{du_i}{dt} = \sum_j m_j \left(\frac{p_i}{\rho_i^2} + \frac{1}{2} \Pi_{ij}\right) (\mathbf{v}_i - \mathbf{v}_j) \cdot \nabla_i W_{ij} . \tag{9}$$

Here again, Π_{ij} is the artificial viscosity, while the rest of the expression represents one of many possible ways of estimating the local "$p\,dv$" work, $-(p\nabla \cdot \mathbf{v}/\rho)_i$ (cf. Monaghan 1985).

The set of equations (1)–(9) provides *three conservation laws*, which we can identify with momentum conservation, energy conservation, and the second law of thermodynamics. If we define the *total momentum* of the fluid as $\mathbf{P} \equiv \sum_i m_i \mathbf{v}_i$, then from equation (6),

$$\frac{d\mathbf{P}}{dt} = -\sum_{ij} m_i m_j \left[\left(\frac{p_i}{\rho_i^2} + \frac{p_j}{\rho_j^2}\right) + \Pi_{ij}\right] \nabla_i W_{ij} = 0 , \tag{10}$$

since $\nabla_i W_{ij} = -\nabla_j W_{ji}$. Similarly we define the *total energy* of the fluid, in the absence of gravity, as $E \equiv \sum_i (m_i v_i^2/2 + m_i u_i)$, and find, using both equations (6) and (9), that

$$\frac{dE}{dt} = \frac{1}{2} \sum_{ij} m_i m_j (\mathbf{v}_i - \mathbf{v}_j) \cdot \nabla_i W_{ij} \left(\frac{p_i}{\rho_i^2} - \frac{p_j}{\rho_j^2}\right) = 0 , \tag{11}$$

since the last three factors are all antisymmetric. Finally, the *specific entropy* at $\mathbf{r}_i$ is defined as $s_i \equiv \log(p_i/\rho_i^\gamma)$ and we find, after some algebra, that

$$\frac{ds_i}{dt} = \frac{1}{2u_i} \sum_j m_j \Pi_{ij} (\mathbf{v}_i - \mathbf{v}_j) \cdot \nabla_i W_{ij} , \tag{12}$$

which is zero when the artificial viscosity $\Pi_{ij} = 0$, and represents a discretized version of the second law of thermodynamics. We could have solved equation (12) instead of equation (9) to obtain the time evolution of the internal energy (as in Benz & Hills 1987). Note, however, that, in deriving equation (12), we have neglected terms proportional to the time derivative of h_i. Therefore, even in the absence of artificial viscosity, the total entropy of the system will not be strictly conserved if the particle smoothing lengths are allowed to vary in time. Had we used equation (12) instead of equation (9) to evolve the system, the total entropy would then be strictly conserved, but not the total *energy*. There are many other equivalent forms of the basic SPH equations (1)–(9), i.e., many forms which all reduce to the correct fluid equations in the limit $N \to \infty, h_i \to 0$. However, most of them will satisfy their associated conservation equations only *approximately*, i.e., up to errors which only tend to zero in the limit $N \to \infty, h_i \to 0$. Instead, our choice of equations has the virtue of conserving energy and momentum exactly, *independent of the number of particles used*. Of course, in the numerical solution, errors will still be introduced by the time-integration scheme.

To provide reasonable accuracy, the SPH method requires the use of large numbers of particles (typically $N \gg 1000$). This rules out a direct summation method (as that used in Paper I) for calculating the gravitational field of the system. In stellar dynamics calculations, tree-based methods have been used with great success to deal with large numbers of particles (see, e.g., Hernquist 1987). Hernquist & Katz (1989) have recently developed a SPH code where gravity is calculated using a tree-based method. From a fundamental point of view, however, calculating the exact gravitational field of the set of discrete SPH particles, viewed as point masses, does not appear desirable to us. Indeed, the physical system here is a fluid, not a collection of discrete entities. The exact gravitational field of the point masses contains all the small scale particle-to-particle interactions, which are in this case entirely spurious. For these reasons, we have turned instead to a grid-based method for calculating the smooth gravitational field of the fluid. The SPH definition of the (smooth) density (eq. [2]) is used to calculate the values of the source term for Poisson's equation at grid points. An FFT–based convolution algorithm (Hockney & Eastwood 1988; Wells et al. 1990) is used to solve for the gravitational potential on the grid. Forces at grid points are obtained by finite differencing and then interpolating onto the particle positions.

The time-evolution equations (1) are integrated using an explicit leapfrog scheme. This provides second-order accuracy in time. Note that such a low-order scheme (instead of the direct N-body code's typical high-order scheme; cf. Aarseth 1985) is appropriate here because pressure gradient forces are subject to numerical noise. For stability, the timestep must satisfy a Courant condition with h_i replacing the usual grid separation. For accuracy, the time step must also be a small enough fraction of the system's dynamical time. In practice we calculate the timestep as in Monaghan (1989), i.e., $\Delta t = \mathrm{Min}\,(\Delta t_1, \Delta t_2)$ with

$$\Delta t_1 = k\ \mathrm{Min}_i \left(\frac{h_i}{c_i + 1.2\alpha c_i + 1.2\beta\ \mathrm{Max}_j\ \mu_{ij}} \right), \tag{13}$$

where $k \approx 0.1$, and $\Delta t_2 = \mathrm{Min}_i\,(h_i/\dot{v}_i)^{1/2}$.

The use of time-dependent, individual particle smoothing lengths h_i is essential in ensuring that the spatial resolution remains acceptable throughout a calculation. The local values of h_i must continually adapt themselves to expanding and contracting regions of the fluid. It is convenient, in practice, to continually update the values of h_i so that the *number of nearest neighbors*, N_N, of any particle remains approximately constant (and $\gg 1$). This number is a very important parameter in the calculation: it is directly related to the local level of numerical noise in the system. For three-dimensional calculations, we have found that N_N must be at least $64(=4^3)$. In our code, nearest neighbor searching is done using the grid-based algorithm of P^3M codes (Hockney & Eastwood 1988). This algorithm proved extremely efficient, even for wide distributions of smoothing lengths, provided that one is careful to fine-tune the ratio $L/\langle h_i \rangle$ of the grid separation L to the average particle smoothing length $\langle h_i \rangle$. For a typical collision calculation with $N \sim 10^4$ and $N_N \sim 10^2$, the CPU time is $\sim$10 hr on an IBM 3090–600J supercomputer. Depending on the parameters of the run, about 50%–90% of the CPU time is spent updating nearest neighbor lists, while most of the rest is taken by the calculation of the gravitational field.

2.2. *Test Calculations*

Here we present the results of several test calculations which we performed to verify the accuracy of our numerical method. Only the calculations which are directly relevant to the problem studied in this paper will be described here in detail. A more complete discussion of our method, together with a number of other test calculations, will be published elsewhere (Rasio & Shapiro 1991).

2.2.1. *Shock-Tube Calculations*

The one-dimensional Riemann shock-tube calculation of Sod (1978) has become a widely accepted standard test of numerical hydrodynamics codes. Figure 1 presents the results of this calculation using SPH with $N = 3000$ particles. At $t = 0$, an interface located at $x = 0$ separates two fluids. The fluid on the left has density $\rho_l = 1.0$ and pressure $p_l = 1.0$, while on the right $\rho_r = 0.25$ and $p_r = 0.1795$. The figure shows the density and velocity profiles at $t = 0.15$. An adiabatic equation of state was assumed with $\gamma = 1.4$. Employing the artificial viscosity of equation (7), we obtained a very good representation of the shock for $\alpha = \beta = 2.0$ and $\eta^2 = 0.01$. Discontinuities are smoothed over a width $\approx 2h_i$, as expected, but no unphysical oscillations appear. The results were also best when the density was represented by varying the number density of equal mass particles, as opposed to varying the particle masses while keeping their number density uniform. The smoothing lengths h_i were allowed to vary both in space and time, in order to maintain a constant number of nearest neighbors $N_N \approx 16$ for all particles at all times.

A quasi-analytic solution for this problem is easily constructed using standard techniques (see, e.g., Courant & Friedrichs 1976). At any time $t > 0$, five regions of fluid with different thermodynamic states coexist. These regions are separated by the head and tail of the left-propagating rarefaction wave, and the right-propagating shock and contact discontinuity. The solution can be expressed as follows:

$$\rho(x, t) = \begin{cases} \rho l\,, & x \le -c_l t\,, \\ \rho_l[-\mu^2(x/c_l t) + (1-\mu^2)]^{2/(\gamma-1)}\,, & -c_l t < x \le -v_T t\,, \\ \rho_{ml}\,, & -v_T t < x \le v_m t\,, \\ \rho_{mr}\,, & v_m t < x \le v_S t\,, \\ \rho_r\,, & x > v_S t\,, \end{cases} \tag{14}$$

$$p(x, t) = \begin{cases} p_l\,, & x \le -c_l t\,, \\ p_l[-\mu^2(x/c_l t) + (1-\mu^2)]^{2\gamma/(\gamma-1)}\,, & -c_l t < x \le -v_T t\,, \\ p_m\,, & -v_T t < x \le v_S t\,, \\ p_r\,, & x > v_S t\,, \end{cases} \tag{15}$$

$$v(x, t) = \begin{cases} 0\,, & x \le -c_l t\,, \\ (1-\mu^2)(x/t + c_l)\,, & -c_l t < x \le -v_T t\,, \\ v_m\,, & -v_T t < x \le v_S t\,, \\ 0\,, & x > v_S t\,. \end{cases} \tag{16}$$

1991ApJ...377..559R

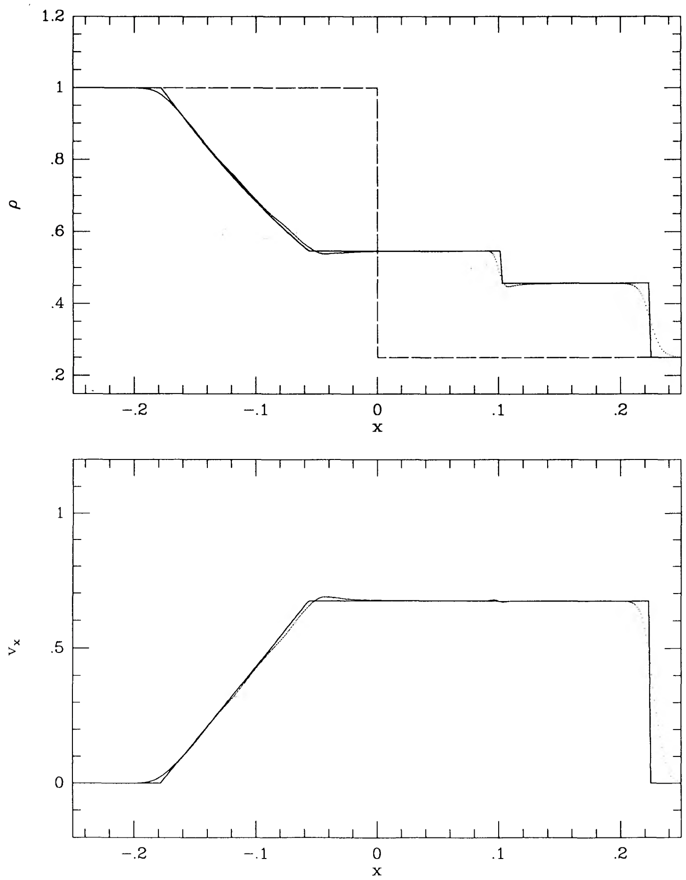

FIG. 1.—Density and velocity profiles for the one-dimensional shock-tube test. The solid line represents the analytic solution (eqs. [14]–[16]). The dotted line is the numerical result using one-dimensional SPH with 3000 particles of equal mass. The dashed line shows the density at $t = 0$.

Here $\mu^2 = (\gamma - 1)/(\gamma + 1)$, $c_l = (\gamma p_l/\rho_l)^{1/2}$ and $c_r = (\gamma p_r/\rho_r)^{1/2}$ are the speeds of sound, v_T is the speed of propagation of the rarefaction wave's tail, and v_S is the shock speed. The postshock pressure p_m is calculated by solving (numerically) the following nonlinear equation, obtained by matching the possible postshock states with the possible postrarefaction wave states,

$$\left(\frac{p_m}{p_r} - 1\right)\sqrt{\frac{1 - \mu^2}{\gamma(p_m/p_r + \mu^2)}} - \frac{2}{(\gamma - 1)}\frac{c_l}{c_r}\left[1 - \left(\frac{p_m}{p_l}\right)^{(\gamma - 1)/2\gamma}\right] = 0\,, \tag{17}$$

over the interval $[p_r, p_l]$. The density on the left of the contact discontinuity is $\rho_{ml} = \rho_l(p_m/p_l)^{1/\gamma}$, since the fluid there is adiabatically connected to the left. The postshock fluid velocity v_m is obtained from the rarefaction wave equations as

$$v_m = \frac{2c_l}{(\gamma - 1)}\left[1 - \left(\frac{p_m}{p_l}\right)^{(\gamma - 1)/2\gamma}\right], \tag{18}$$

and from equation (16), we then get $v_T = c_l - v_m/(1 - \mu^2)$. Mass conservation across the shock gives the shock velocity

$$v_S = \frac{v_m}{1 - \rho_r/\rho_{mr}}\,. \tag{19}$$

Finally, the postshock density ρ_{mr} is calculated by the usual Hugoniot relation,

$$\rho_{mr} = \rho_r\left(\frac{p_m + \mu^2 p_r}{p_r + \mu^2 p_m}\right). \tag{20}$$

This analytic solution is also shown in Figure 1, for $t = 0.15$.

For the above calculation we employed a special, *explicitly one-dimensional version* of our code. While such a calculation is useful to establish the validity of the method a priori, it does not present a realistic assessment of how accurate the results of an actual *three-dimensional* calculation will be. At issue is not only the much smaller number of particles per dimension and reduced spatial resolution in a three-dimensional calculation. Many sources of numerical errors, such as the interpenetration and diffusion of particles, are artifically reduced when motion with only one degree of freedom is allowed.

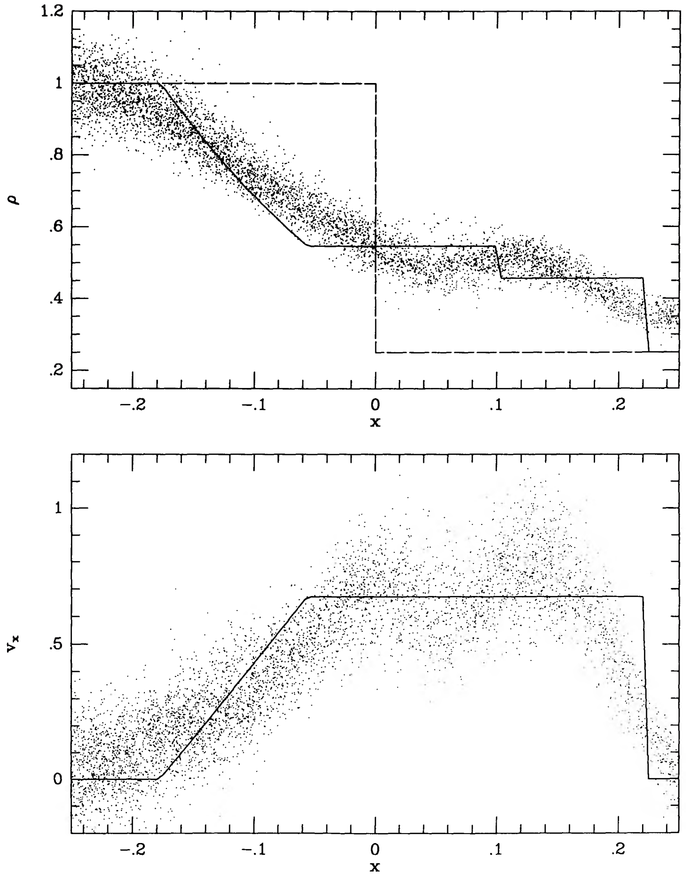

FIG. 2.—Results of the same one-dimensional shock-tube calculation shown in Fig. 1, but now using three-dimensional SPH with $N = 10^4$ particles of equal mass. One dot is plotted for each particle in the calculation (see text).

To illustrate this point better, we now consider a different kind of test, which uses the fully three-dimensional version of our code. The physical problem, however, remains exactly the same: at $t = 0$, two semi-infinite regions of fluid are separated by a plane interface located at $x = 0$. The thermodynamic states in the two regions are the same as above. Periodic boundary conditions on the four planes $y = \pm L$ and $z = \pm L$ are imposed, adopting a technique often employed in molecular dynamics (cf. Allen & Tildesley 1989). The condition $L \gg \text{Max}_i\,(h_i)$ is satisfied throughout the calculation, so that the exact position of the boundary planes has no effect on the numerical results.

Figure 2 shows the results of the calculation. Here we used $N = 10^4$ equal-mass particles, with a constant number of nearest neighbors $N_N \approx 100$. The calculation takes place in a cubic box with $L = 1.0$ and periodic boundary conditions are imposed on all sides. Just as would be the case in a typical simulation, the particles are randomly distributed within each constant-density region and the features we examine (shock front, rarefaction wave, etc. . . .) involve only a small fraction of the total number of particles. It is clear that, in an average sense, there is still good agreement with the analytic solution, but the spatial resolution is rather poor and there is considerable numerical noise. Note that by placing the particles on a regular lattice at $t = 0$, one can easily reduce the numerical noise (cf. § 2.2.2 below). This is especially true if one is careful to align the plane of the discontinuity with a face of the lattice. However, we feel that such a set-up is very artificial and not representative of the particle distributions encountered in the course of a typical SPH calculation.

We have performed several other one-dimensional test calculations involving simple waves, using both the one-dimensional and three-dimensional versions of our code. These included free expansion calculations, useful for testing the numerical method in cases where the fluid density decreases to zero, and head-on collisions of two fluid slabs, used to check the ability of our code to calculate strong shocks. We also designed a *two-dimensional* version of the code, which was tested on the classical problem of the interaction between a shock front and an oblique contact discontinuity. In all cases the numerical results were checked against analytical or semianalytical solutions and good agreement was found, with the level of accuracy similar to that which is shown in Figures 1 and 2. Since these calculations are not directly relevant to the problem considered in this paper, we do not describe them here in detail.

2.2.2. *Stability of a Polytrope*

We have checked very carefully the ability of our SPH code to maintain a given hydrostatic, self-gravitating structure in stable dynamic equilibrium. In particular, we performed extensive tests on a spherical, nonrotating polytrope of index $n = 3/2$; this configuration will be used again in the next two sections of the paper. In one calculation, the dynamical evolution of the polytrope was followed all the way from time $t = 0$ to time $t = 15$ (here time is in units of $[R^3/GM]^{1/2}$, where M is the total mass and R is the radius of the configuration). No deviation from the initial profile was found, apart from a very small amplitude ($\lesssim h_i$) oscillation of the surface. Numerically, the mass profiles at $t = 0$ and $t = 15$ were found to agree to within 2% everywhere. At $t = 0$, in this calculation, the exact density profile of the polytrope was constructed with a distribution of $N = 10^4$ particles with equal masses, but varying number density. The internal energy per unit mass u_i of each particle was everywhere set according to the isentropic condition $u_i = A\rho_i^{\gamma-1}/(\gamma - 1)$, where $A \equiv p/\rho^\gamma$ is a constant. The resulting entropy $s_i = \log(p_i/\rho_i^\gamma)$ is then exactly the same for all particles and remains strictly conserved in the absence of shocks (cf. eq. [12]). The smoothing lengths h_i were adjusted so that each particle interacts with $N_N \approx 100$ neighbors at all times. This number was found to provide an acceptable compromise between good spatial resolution and low numerical noise.

Alternatively, one can construct the density profile at $t = 0$ by varying the individual masses of the particles, but keeping their number density uniform. This has the advantage of providing a uniform spatial resolution in the calculation. Moreover, by placing the particles on a regular grid at $t = 0$, we find that the numerical noise can be considerably reduced (cf. Monaghan 1985). We will use this approach in the following section, where we study the tidal perturbation of polytropes. In the rest of the paper, however, we will often be dealing with calculations of the long-term evolution of a system where the fluid is rather violently perturbed. In those cases, the carefully arranged distribution of particle masses is eventually destroyed and it proves better to work with particles of equal mass.

2.2.3. *Tidal Encounters between a Point Mass and a Polytrope*

Many analytical calculations of tidal encounters between a polytrope and a point mass have been performed using the method of Press & Teukolsky (1977, hereafter PT). These calculations (Lee & Ostriker 1986; Gierz 1986; McMillan et al. 1987; Ray et al. 1987) are based on linear perturbation expansions in terms of the normal modes of oscillation of the polytrope. A sensitive test for any hydrodynamical code used for studying stellar collisions is its ability to reproduce the analytical results of the PT calculations in the limit of large periastron separations.

Here we set up an $n = 3/2$ polytrope with $N = 10^4$ particles as described in the previous section, with the density profile represented by varying the individual particle masses. This procedure maintains good spatial resolution throughout of the star. As before, we adopt units in which $G = M = R = 1$. At $t = 0$, a point perturber with mass $m = 1$ is placed on a parabolic trajectory, at a distance $d = 5$ from the center of the star. As the calculation proceeds, we monitor the transfer of energy from the orbit to the fluid. This is illustrated in Figure 3 for an encounter with periastron distance $r_p = 2$. Note that throughout this paper, r_p will be defined as the periastron distance of the *unperturbed orbit* on which the point mass is placed at $t = 0$. The minimum separation actually reached will therefore always be less than r_p. The orbital energy is calculated as $E_{\rm orb} \equiv \mu v_r^2/2 + \phi$, where μ is the reduced mass, v_r is the relative velocity, and ϕ is the gravitational potential energy of interaction between the fluid and the point mass. When the perturber approaches periastron, the orbital energy rather suddenly drops by a certain amount $\Delta E_{\rm orb} = -\Delta E_{\rm fluid}$. This amount can be exactly calculated, in the tidal approximation, by using the PT method. To calibrate our numerical data, we used the results of Lee & Ostriker (1986) for an $n = 3/2$ polytrope to calculate $\Delta E_{\rm orb}$ analytically.

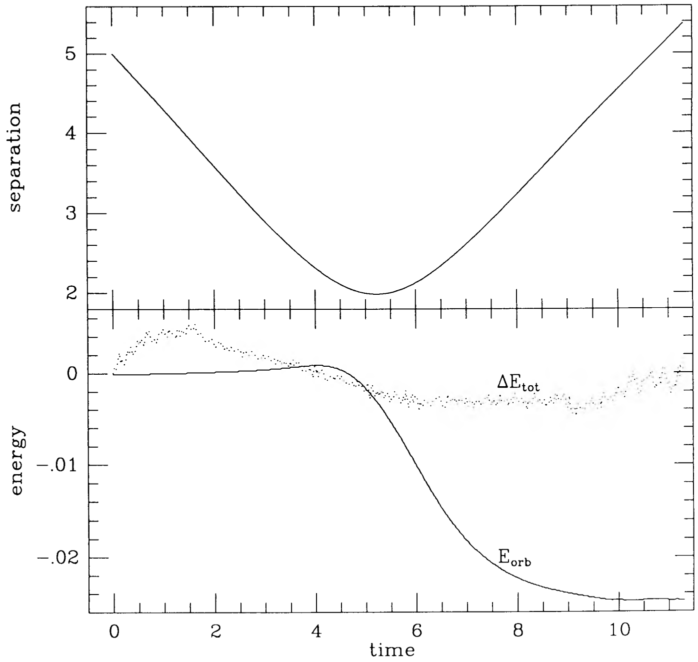

FIG. 3.—Tidal dissipation of orbital energy for a parabolic encounter of a point mass with a polytrope of equal mass and index $n = 3/2$ (units defined by $G = M = R = 1$). The periastron separation of the unperturbed orbit was $r_p = 2$. The solid line shows the orbital energy $E_{\rm orb}$. The dotted line shows $\Delta E_{\rm tot} = E_{\rm tot}(t) - E_{\rm tot}(0)$, a measure of the numerical error in maintaining the conservation of total energy during the calculation.

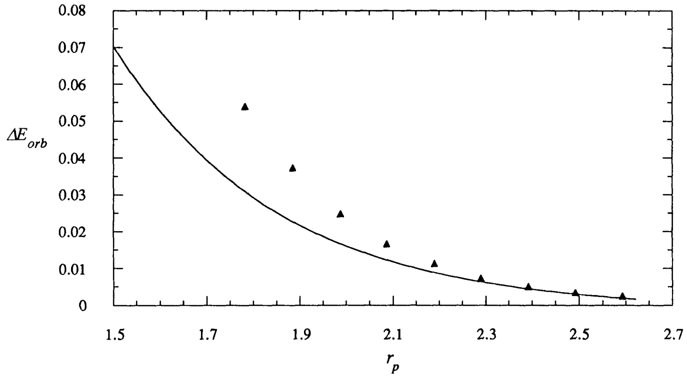

FIG. 4.—Amount of orbital energy $\Delta E_{\rm orb}$ dissipated during the parabolic encounter of a point mass with a polytrope of equal mass and index $n = 3/2$ (units defined by $G = M = R = 1$), as a function of periastron distance r_p. The solid curve is based on the semi-analytic calculations of Lee & Ostriker (1986). The triangles give our numerical results using SPH.

In Figure 4, we show a comparison between our numerical results and the analytical calculation. In the limit of large periastron distance, the agreement is excellent. One should realize that for such distant encounters, the effect we are trying to measure is of very small magnitude, i.e., $|\Delta E_{\rm fluid}/E_{\rm fluid}| \lesssim 10^{-2}$. Note that one must use the calculated $\Delta E_{\rm orb}$, as we have done, and not $\Delta E_{\rm fluid}$, to measure the amount of energy dissipated. This is because the numerical error in $E_{\rm fluid}$ is usually larger than that in $E_{\rm orb}$, which is calculated independently. Empirically, we found that it is in fact quite possible to continue the calculation beyond the point where $\Delta E_{\rm orb}$ becomes comparable to $\Delta E_{\rm tot}$, the numerical error in the conservation of total energy, and still obtain good agreement with the semianalytical results. For the most distant encounter in Figure 4, with $r_p = 2.6$, the analytical and numerical results agree to within $\approx 10\%$. For encounters with $r_p > 2.6R$ numerical errors start contaminating the estimate of $\Delta E_{\rm orb}$ and the agreement becomes worse.

Apart from providing a crucial test of our code, this calculation also gives new information on the onset of nonlinear effects in tidal encounters with polytropes. Figure 4 shows that significant deviations from the PT calculation are already apparent for $r_p \approx 2$. The onset of detectable mass loss from the star occurs at $r_p \approx 1.5$. However, since the critical periastron for capture in a globular cluster is $r_p \approx 3$ (see, e.g., Lee & Ostriker 1986), it is possible for a main-sequence star in a globular cluster to tidally capture a compact object of comparable mass without being immediately disrupted (this does not appear to be the case for giant stars, as we show in § 4). The long-term evolution of the binary after such a nondisruptive tidal encounter depends on how efficiently the tidal energy deposited in the star is thermalized (Ray et al. 1987). This clearly takes place on an internal dissipation timescale and is beyond the scope of our (adiabatic) calculations.

3. COLLISIONS BETWEEN A POINT MASS AND A POLYTROPE

We now extend our study of encounters between a point mass and a polytrope into the regime of direct physical collisions, where nonlinear effects such as shocks and mass transfer dominate the dynamics. Polytropes cannot be used to represent a giant star in any reasonable way. However, preliminary SPH calculations of collisions with polytropes are important, because comparable finite-difference calculations exist. Most recently, Różyczka et al. (1989) have performed high-resolution finite-difference calculations of head-on (axisymmetric) collisions between a polytrope of index $n = 3/2$ and a point mass, and Ruffert & Müller (1990, hereafter RM) have treated the more general, off-axis case.

Our assumptions here will be similar to those made by RM. A polytrope of index $n = 3/2$ and mass M is placed on a parabolic orbit with a point mass $m = M$. The polytrope is constructed as in § 2.2.2, using particles of equal mass. A softened gravitational potential is used to calculate the interaction between the point mass and the fluid. The softening length is chosen equal to the average particle smoothing length and remains constant throughout the calculation. No special boundary condition is otherwise imposed near the point mass. This is consistent with the fact that the physical size of a compact object could never be resolved in the calculations. Note, however, that the individual particle smoothing lengths do become smaller in the high density region typically found around the point mass. We have studied numerically the importance of the softening length and have found, as did RM, that varying it changes the maximum temperature and density reached very near the point mass, but has practically no influence on the overall dynamics. We have also neglected possible effects due to nuclear burning and radiative cooling. A detailed analysis by Różyczka et al. (1989) indicates that they are indeed dynamically unimportant. The equation of state in the code used by RM was that of a perfect gas plus radiation. Instead, we employ a simple adiabatic equation of state with $\gamma = 5/3$ for our SPH calculations, since radiation pressure was found to be negligible. Specifically, we can write the ratio $\beta \equiv aT^4/(2\rho u)$ of radiation to gas pressure at r_i as $\beta_i = 1.2 \times 10^{-3}(M/M_\odot)^2 u_i^3/\rho_i$, with u_i and ρ_i in units where $G = M = R = 1$. We find that the total mass of particles with $u_i^3/\rho_i > 10^2$ (i.e., for which the radiation pressure would represent more than a $\sim 10\%$ correction to the equation of state) was always $< 10^{-2}$ in our calculations.

We can extend to collisions the point of view adopted for tidal encounters, i.e., study the transfer of orbital energy to the fluid (Fig. 5). However, the concept of "orbital" becomes meaningless here after a true collision. Indeed, consider a sequence of encounters with decreasing periastron distances r_p (recall that "periastron distance" here refers to the unperturbed parabolic orbit). The sequence can be divided into two regimes, according to the qualitative outcome of the collision. For encounters with $0.6 \lesssim r_p \lesssim 1.5$,

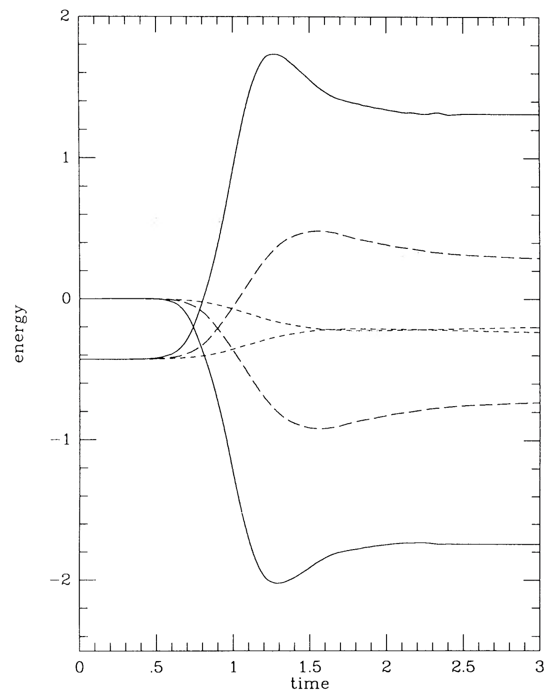

FIG. 5.—Transfer of orbital energy to the fluid for parabolic collisions between an $n = 3/2$ polytrope and a compact object of equal mass (units defined by $G = M = R = 1$). The solid, long-dashed, and short-dashed lines correspond to collisions with $r_p = 0$, $r_p = 0.5$, and $r_p = 1$, respectively. In each case, the upper curve shows the total fluid energy $E_{\rm fluid}$, while the lower curve shows the orbital energy $E_{\rm orb}$.

which we will call "near-grazing" encounters, we find that the star is not entirely disrupted. Only a small quantity of gas is extracted from the outer layers. Part of the extracted gas remains bound to the point mass perturber, while the rest escapes to infinity. Three components are therefore produced in this type of encounter: (1) the perturbed star; (2) the point mass, now surrounded by a gaseous disk; and (3) an expanding shell of gas. Since the initial orbit is parabolic, components (1) and (2) will be bound on a very eccentric elliptic orbit. All three components have acquired some of the lost orbital angular momentum. For encounters with $0 \leq r_p \lesssim 0.6$, which we will call "near–head-on" collisions, the star is completely destroyed and only two components remain after the encounter. A significant fraction of the gas remains bound to the point mass, forming a massive disk around it, while the rest escapes and forms an expanding shell. Our calculations reveal that the transition between the two types of encounters is rather abrupt: between $r_p = 0.75$ and $r_p = 0.6$, the amount of gas captured by the perturber increases by more than an order of magnitude (cf. below). The same two basic types of encounters were identified by RM, though they did not attempt to locate the transition accurately.

Figure 6 shows density contours and the velocity field at various times for a head-on collision. Time is in units of $(R^3/GM)^{1/2}$, or, equivalently, 1.6×10^3 s $(R/R_\odot)^{3/2}$ $(M/M_\odot)^{-1/2}$. Velocity vectors are calculated on a regular grid, in the center of mass frame of the system. At $t = 0.25$, just before impact, the two objects are approaching each other with velocity $|v(t = 0.1)| = 360$ km s^{-1} $(R/R_\odot)^{-1/2}(M/M_\odot)^{1/2}$ (the velocity scale remains the same in all frames). There are 16 density contours, spaced logarithmically, and covering eight decades down from the maximum. At $t = 0.5$ the point mass enters the star, and by $t = 0.75$ a bow shock is clearly apparent. The opening angle of the bow shock is $\approx 90°$, which is expected, given the relatively low Mach numbers $\mathscr{M} \gtrsim 1$ reached during parabolic impacts. Gas that has passed through the shock reexpands behind the point mass. Part of it simply accelerates away from the star along the axis of the collision, but part of it also spreads rapidly around the star in the forward direction, catching up with the shock. The geometry of the outflow agrees well with that found in finite-difference calculations (cf. Fig. 1*a* of RM). When the shock reaches the center of the star, the character of the flow around the point mass is changed. The direction of the flow near the axis is reversed, from backward to forward, so that the point mass is now almost comoving with the fluid in its vicinity. Simultaneously, two counterrotating vortices appear on each side of the point mass. This begins to be apparent at $t = 1.0$ but is seen most clearly at $t = 1.25$ in Figure 6. An identical behavior is found in finite-difference calculations by Różyczka et al. (1989; cf. their Fig. 2*c*) as well as investigations of axisymmetric accretion flows by Fryxell, Taam, & McMillan (1987) and Shima, Matsuda, & Inagushi (1986). It is encouraging to see that in spite of its low spatial resolution, our SPH calculation does reproduce correctly such small features of the flow. By $t = 1.5$, the shock has propagated through the entire star and most of the fluid is now accelerating radially outwards. The particle plots on Figure 7 illustrate the long-term evolution of the system.

Even for small r_p, the dynamics of off-axis collisions appears very different from the head-on case. This is because the orbital angular momentum is transferred very effectively to the fluid. Moreover, the angle of incidence of the trajectory onto the stellar surface, $i = \sin^{-1}(r_p/R)^{1/2}$, increase rather rapidly with r_p. The geometry of the flow will therefore be modified by even small deviations from the precisely head-on situation. Figure 8 shows the hydrodynamics of the impact for a trajectory with $r_p/R = 1/4$.

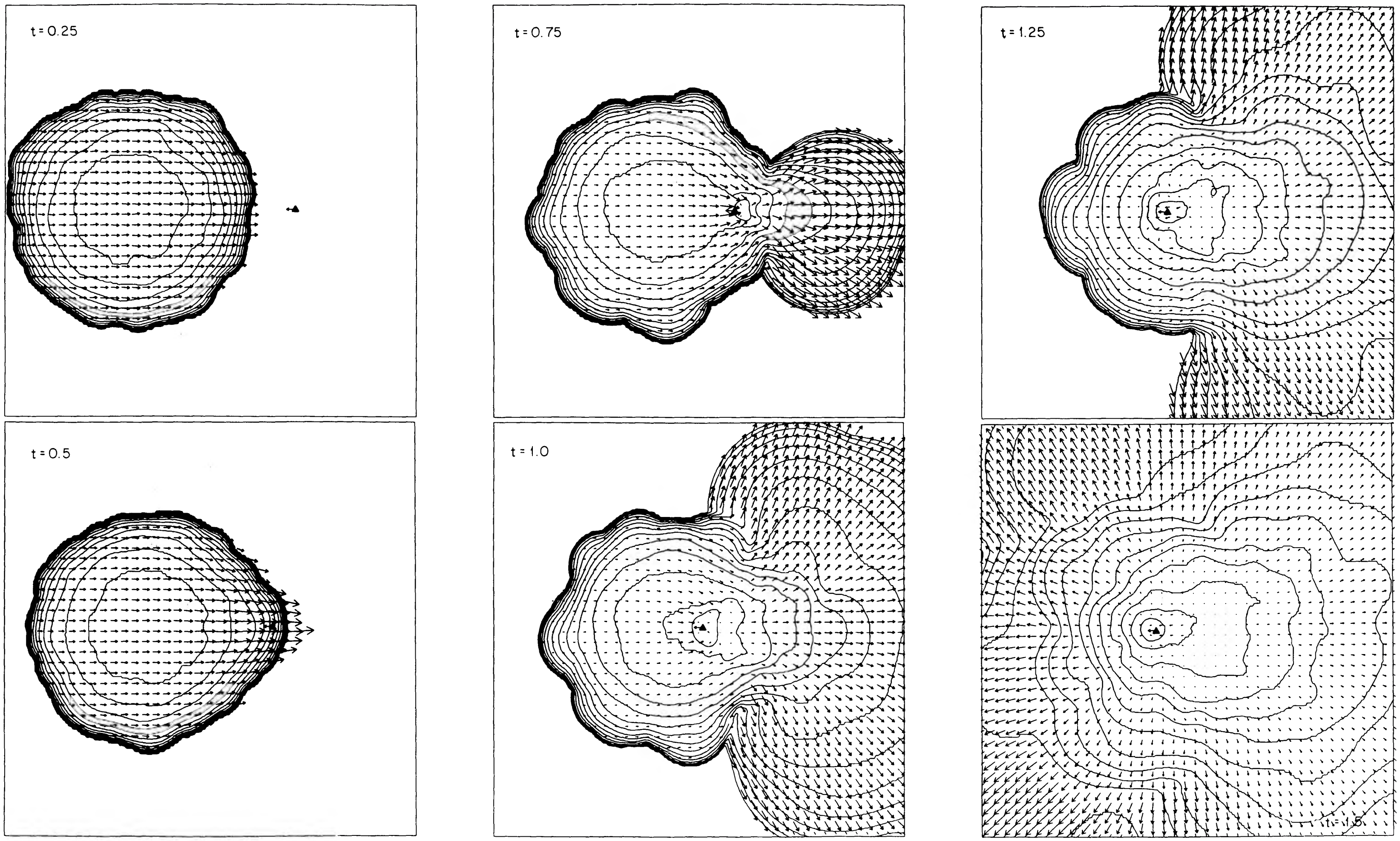

FIG. 6.—Density contours and velocity field at various times in the orbital plane for the head-on, parabolic collision of a polytrope of index $n = 3/2$ with a compact object of equal mass. The triangular dot represents the compact object, placed initially one stellar radius above the stellar surface (units are defined by $G = M = R = 1$). See text for details.

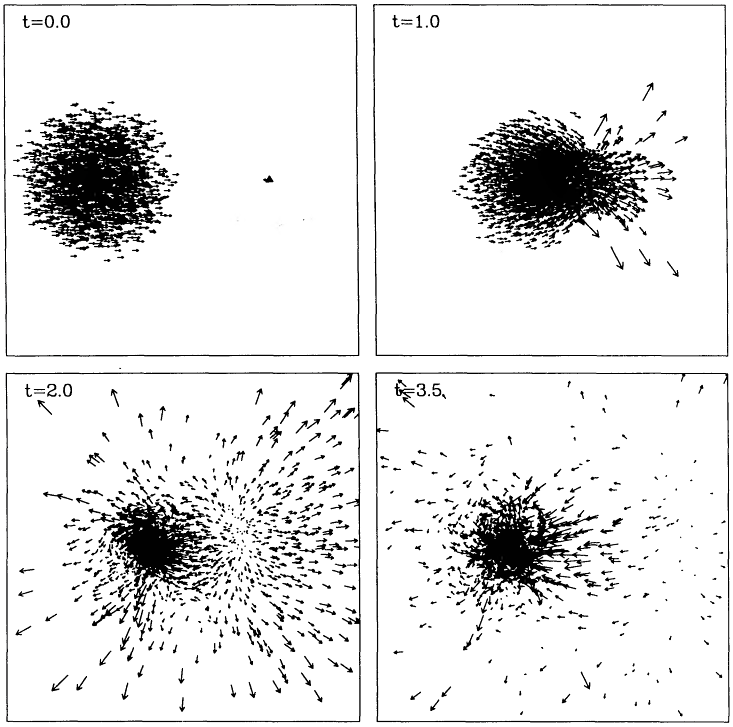

FIG. 7.—Particle plots for the same head-on collision shown in Fig. 6. All particles shown are in the orbital plane, i.e., have $z_i < 2h_i$.

Conventions are as in Figure 6. Note that the reexpansion of the shock-heated gas is no longer symmetrical with respect to the direction of motion of the point mass. As in the head-on case, the gas also flows along the stellar surface, but here this occurs only on one side. At $t = 1.5$, the point mass has reached periastron, in the sense that its velocity vector has been rotated by 90° since $t = 0$. We see that a single large vortex has formed around it. About half of the star has been disrupted at this point. By $t = 2.0$, the shock has propagated through the remaining half, and the star is completely destroyed. The particle plots of Figure 9 better illustrate the final state of the system, which consists of the point mass embedded in a massive, rapidly rotating, thick disk of gas (see below).

For the off-axis collision also, the SPH results agree well qualitatively with those of a finite-difference calculation (cf. RM, Fig. 2). However, comparing our Figures 6 and 8 with Figures 9 and 10 of RM (which show their calculations repeated with grids of varying sizes) clearly indicates that a finer spatial resolution can be obtained with a finite-difference code. To achieve the same *overall* spatial resolution as that of a finite-difference calculation on a 128^3 grid, SPH would require a number of particles $N > 10^6$, which is clearly not feasible with present computers. Finite-difference calculations are therefore best suited to a detailed study of the hydrodynamics of the impact. However, because SPH allows the evolution of the system to be calculated over a much longer time scale, the final values of many *global properties* of great astrophysical interest, such as the amount of mass ejected from the system, can be accurately determined. In the finite-difference calculations of RM, these quantities could only be determined very roughly by extrapolating from a very early stage in the evolution. Moreover, the particle smoothing lengths in the SPH calculation can adaptively decrease in the high-density region around the point mass so that, as we noted above, the spatial resolution obtained in that region of the flow can in fact be quite good.

Consider the determination of these global properties for the various components that result from the collision. First, we must decide to which component a given SPH particle should be assigned. This turns out to be a nontrivial problem. Even in cases where one can easily separate "by eye" the various components (as in Fig. 9, where the rotating gas cloud can be clearly identified), this assignment proves difficult in practice. The general method which we have adopted is as follows. For each particle i and each component n, we calculate the "enthalpy per unit mass" of the particle with respect to that component as

$$h_i^{(n)} \equiv \tfrac{1}{2}(\boldsymbol{v}_i - \boldsymbol{v}_{\rm CM}^{(n)})^2 + \gamma u_i + \phi^{(n)}(\boldsymbol{r}_i) \, . \tag{21}$$

Here $\boldsymbol{v}_{\rm CM}^{(n)}$ is the center of mass velocity for component n, and $\phi^{(n)}$ is the gravitational potential due to the mass in component n. If $h_i^{(n)}$ is negative for only one n, we assign the particle to that component. If $h_i^{(n)}$ is negative for more than one component, we assign the particle to the component for which $h_i^{(n)}$ is minimum. If $h_i^{(n)}$ is positive for all components, the particle is part of the escaping gas. Clearly, this assignment must proceed by interations, since quantities such as $\boldsymbol{v}_{\rm CM}^{(n)}$ and $\phi^{(n)}$ depend on which particles have been assigned to component n. Convergence is reached when the distribution of particles among the various components no longer changes from one iteration to the next. This method is not unique, but we find that it works very well, in the following sense. First, when the various components are well separated spatially, the assignment always agrees with the distribution that one would choose "by eye." Secondly, its *predictive power* is very good: in most cases it can reliably identify the various components *well before* they are well separated spatially. Note, however, that the method does have some restrictions. In particular, we need to specify a

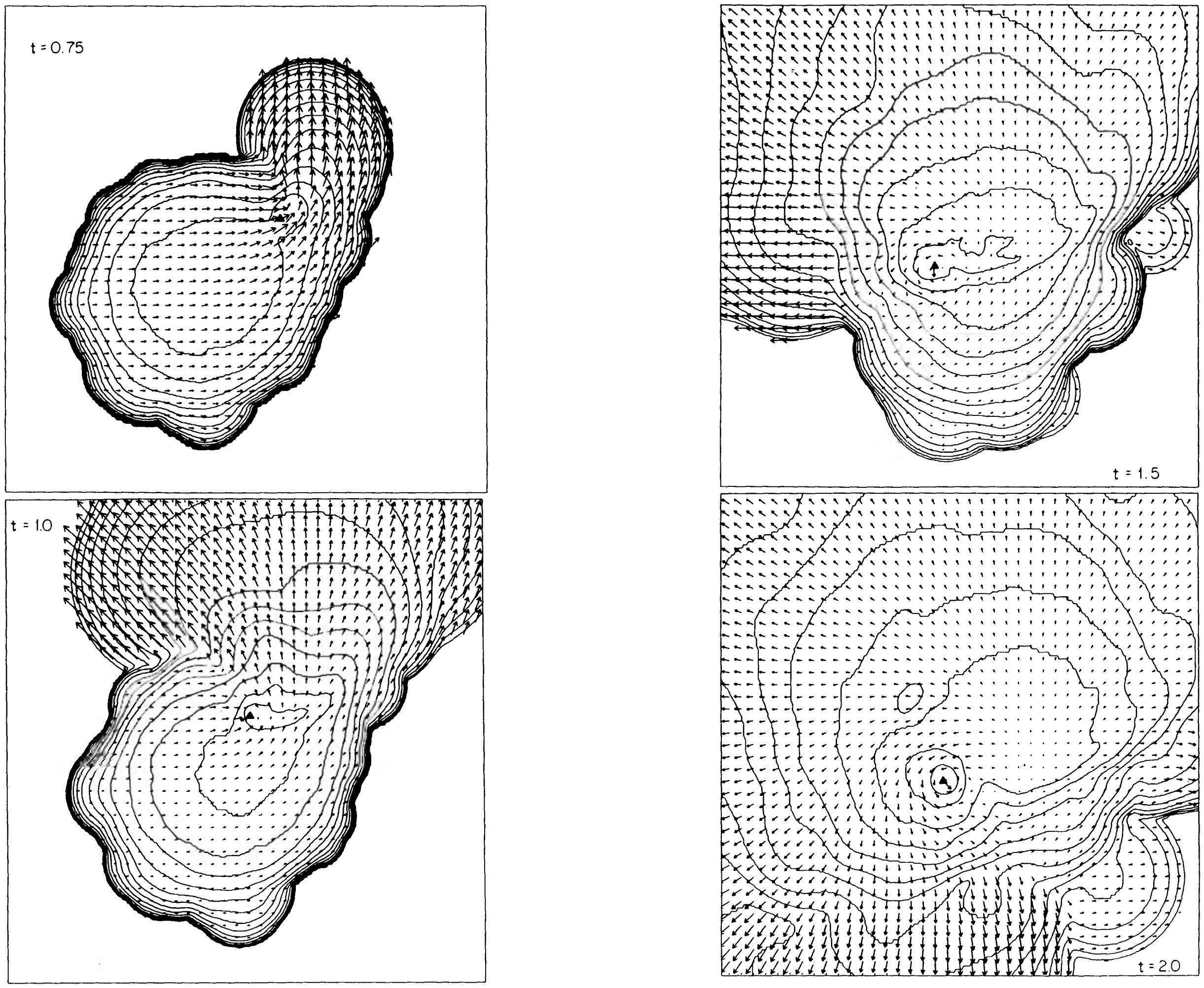

FIG. 8.—Same as Fig. 6, but for an encounter with $r_p = 0.25$

priori how many components there are, and we need to start with a good guess as to where to find them. In practice, we always use the results of the previous time step to determine initial guesses. The method then usually converges in just a few iterations, and never more than about ten.

Table 1 summarizes the results of our long-time calculations. For each bound component, we give the total mass (M_n), angular momentum with respect to the center of mass (J_n), and rms particle separations, both in the orbital plane ($r_n \equiv 0.5\langle x_i^2 + y_i^2\rangle_n^{1/2}$) and perpendicular to the orbital plane ($z_n \equiv \langle z_i^2\rangle_n^{1/2}$). The two components in this case are the massive disk around the compact object ($n = 1$) and the gas that remains bound to the star ($n = 2$). When $M_2 \neq 0$, i.e., when the star is not completely disrupted, the orbital parameters of the binary are also given. These calculations were typically 5–10 times longer than those shown in Figures 7 and 8.

TABLE 1

NUMERICAL RESULTS FOR $n = 3/2$ POLYTROPE[a]

	DISK				STAR				ORBIT		
r_p[b]	M_1	J_1	r_1	z_1	M_2	J_2	r_2	z_2	P_{orb}	e	r_p
0.0..........	0.72	0.00	0.7	0.7	0.00	...	...	...	...	...	...
0.25.........	0.81	0.41	1.0	0.7	0.00	...	...	...	...	...	...
0.50.........	0.84	0.71	1.2	0.7	0.00	...	...	...	...	...	...
0.60.........	0.87	1.00	1.4	0.7	0.00	...	...	...	...	...	...
0.75.........	0.06	0.05	1.0	0.7	0.84	0.09	0.8	0.6	11.	0.67	0.58
1.0..........	0.03	0.03	1.0	0.5	0.93	0.13	0.6	0.4	20.	0.70	0.81
1.50.........	0.003	0.003	0.6	0.2	0.98	0.08	0.4	0.3	73.	0.77	1.45

[a] Units are such that $G = M = R = 1$.

[b] Periastron separation of the unperturbed initial orbit.

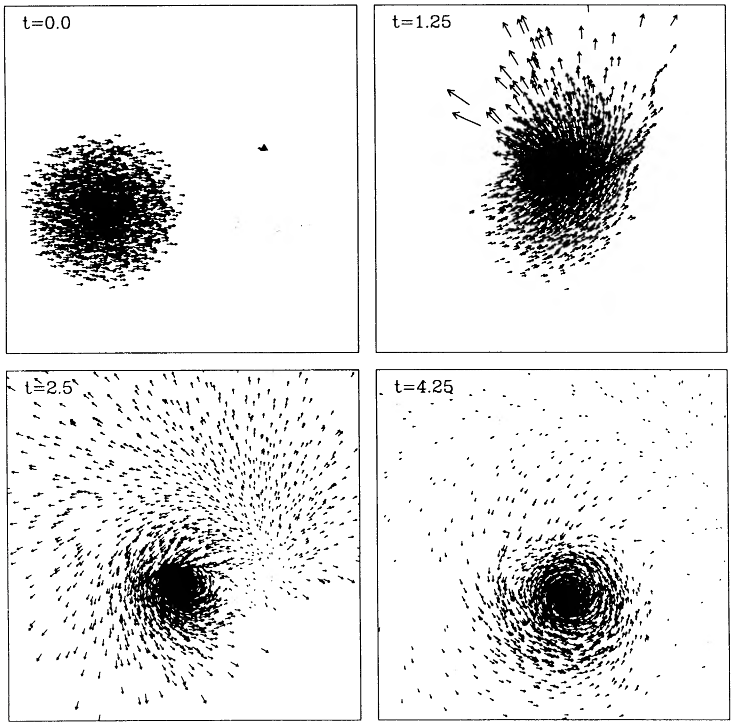

FIG. 9.—Same as Fig. 7, but for an encounter with $r_p = 0.25$

The relative rates of change of the masses and angular momenta listed in Table 1 have typically become $\lesssim 10^{-2}$ by the end of the calculations. The rms separations, however, are not really global conserved quantities and may still be varying slightly. They are given only as a crude indication of the geometric shape of the components.

In order to determine how sensitive our results are to the number of particles used in the code, we have repeated a "standard" calculation with an increasing number of particles. Specifically, the amount of mass loss in a head-on collision was recalculated several times with different particle numbers. The results appear in Table 2. If we estimate the error by taking the difference between the results obtained with the two largest numbers of particles, we conclude conservatively that 30% ± 1% of the stellar mass is ejected. For comparison, RM could only determine a lower limit of 12%, based on finite-difference calculations with a 64^3 grid.

From the point of view of binary formation, an important consequence of these results is that even for near-grazing collisions, with $0.7 \lesssim r_p/R \lesssim 1.5$, a significant expansion of the star takes place during the first close passage. Moreover, the periastron distance of the subsequent orbits decreases as more and more orbital energy gets transferred to the gas. Complete destruction of the star is therefore expected to occur after just a few orbits. We conclude that for polytropes, only the more distant tidal captures, with $r_p/R > 1.5$, could lead to the formation of a long-lived binary (see, however, the discussion in § 5). We did not calculate the long-term orbital evolution of the system in order to verify this directly, but we did so for red giants, as described in the next section.

4. COLLISIONS BETWEEN A POINT MASS AND A GIANT STAR

In this section, we present the results of our calculations of parabolic encounters between a giant star and a point mass. Our basic approach will be very similar that of § 3 for collisions with a polytrope. Here, however, because we are primarily interested in binary formation, we will place more emphasis on the long-term and orbital evolution of the system. We performed two types of calculations: one using large numbers of particles, up to $N = 4 \times 10^4$, and focusing on the detailed hydrodynamics of the initial interaction, the other type using a smaller number of particles, $N = 8 \times 10^3$, and focusing on the long-term evolution following the

TABLE 2

INFLUENCE OF PARTICLE NUMBER

N	M_1
2500.........	0.757
5000..........	0.735
10,000.........	0.716
20,000.........	0.703
40,000.........	0.698

initial impact. In one case we were able to follow the evolution of the binary for seven complete orbital periods, calculating all the subsequent encounters between the two components. If a large enough number of successive encounters can be calculated, one can then try to extrapolate the evolution and determine the final state of the binary. In Paper I, because of the very small number of particles ($N \sim 500$) and simple method used, we were able to follow the evolution of the binaries for a very large number of orbits (~ 100) and directly calculate their final dynamical state. This has not been possible here.

4.1. *Giant Model*

Dynamically, a giant star can be treated as a two-component system: a high-density, degenerate core, surrounded by an extended envelope with a rather flat density profile. The distribution of *mass* in the star is the essential feature here. Other properties, such as temperature and opacity in the envelope or energy generation at the core boundary, can be safely ignored since they will not influence the behavior of the star on a dynamical time scale. We must therefore construct numerically a stable hydrostatic equilibrium configuration whose *mass distribution* correctly represents that of a giant star. A further simplification arises from the very large density contrast between core and envelope (typically $\rho_c/\bar{\rho} \sim 10^{10}$) and small core radius (typically $R_{\rm core}/R_G \sim 10^{-4}$). These characteristics justify the use of a *single point mass* to represent the core.

Stars evolving from the main sequence toward the giant branch describe a one-parameter sequence of models. Joss, Rappaport, & Lewis (1987) have conveniently represented this sequence in terms of a core mass versus radius relation. It would be prohibitively expensive, however, to repeat the calculation of all encounters for many different models along the sequence. Fortunately, for encounters in globular clusters, it will be sufficient to concentrate on just one generic "subgiant" model, representing stars near the base of the giant branch. Indeed, stars evolving off the main sequence will spend a much longer time as subgiants than as evolved red giants, typically $t_{\rm sg}/t_{\rm rg} \sim 100$. Moreover, the small velocity dispersion of stars in globular clusters implies that cross sections are dominated by gravitational focusing and scale only linearly with radius. The ratio of time scales therefore largely compensates for the larger physical size of more evolved stars (typically $R_{\rm rg}/R_{\rm sg} \sim 20$), so that encounters with subgiants are much more frequent than encounters with evolved red giants (see Verbunt & Meylan 1988 for a detailed calculation). This motivates our decision to work only with a "subgiant" model. However, when expressed in terms of nondimensional quantities, our numerical results are in fact little influenced by the details of the giant star's internal structure.

Our generic subgiant star is defined by its core to envelope mass ratio, $M_{\rm core}/M_{\rm env} = 1/3$. For a typical globular cluster giant today, the total mass $M_G = M_{\rm core} + M_{\rm env} = 0.8\ M_\odot$, so that $M_{\rm core} = 0.2\ M_\odot$ and $M_{\rm env} = 0.6\ M_\odot$. The radius of such a star should be $R_G \approx 6\ R_\odot$ (cf. Joss et al. 1987). Throughout this section, we adopt units such that $R_G = M_{\rm env} = G = 1$. The natural unit of velocity for the problem is then

$$\tilde{v} \equiv \sqrt{\frac{GM_{\rm env}}{R_G}} = 140\ {\rm km\ s^{-1}} \left(\frac{M_{\rm env}}{0.6\ M_\odot}\right)^{1/2} \left(\frac{R_G}{6\ R_\odot}\right)^{-1/2}, \tag{22}$$

while the unit of time (dynamical time scale) is

$$\tilde{t} \equiv R_G/\tilde{v} = 8.4\ {\rm hr} \left(\frac{R_G}{6\ R_\odot}\right)^{3/2} \left(\frac{M_{\rm env}}{0.6\ M_\odot}\right)^{-1/2}. \tag{23}$$

Next, we need to construct the density profile of the envelope. This turns out to be nontrivial for an adiabatic equation of state. A natural solution, given that giant star's envelopes are largely convective, would be to "generalize" the polytrope used in § 3, i.e., to place gas with constant specific entropy in hydrostatic equilibrium around the point mass core. The singularity at $r = 0$ can be handled as before by softening the gravitational interaction. Unfortunately, for an adiabatic equation of state with $\gamma = 5/3$, a very steep density profile (roughly $\rho \propto r^{-5}$) results, which does not describe well at all the distribution of mass in an actual giant envelope. Instead, the density profiles of red giant envelopes tend to be fairly flat. In Paper I, we adopted the simple $\rho \propto 1/r$ profile suggested by Tuchman, Sack, & Barkat (1978). Another possibility would be to impose this same $\rho \propto 1/r$ profile here, and to calculate the corresponding pressure resulting from hydrostatic equilibrium. The problem with this approach is that the solution is unstable: a large zone of *convective instability* exists near the stellar surface. Our three-dimensional calculations can very well trigger the unstable g-modes, thereby requiring us to use a stable initial configuration.

Fortunately, a simple modification to the density profile of Paper I will make the solution stable. This can be seen as follows. We impose a density profile near the stellar surface such that $\rho(r) \to {\rm const} \times (R - r)^\nu$ as $r \to R$, while requiring hydrostatic equilibrium and a constant ratio of specific heats γ. A straightforward calculation then gives for the Brunt-Väisälä frequency (see, e.g., Cox 1980) near the surface $\omega_{\rm BV}^2 \equiv (GM/R^2)(1/c_p)(ds/dr) \to (GM/R^2)(R - r)^{-1}[(\nu\gamma - \nu - 1)/\gamma]$ as $r \to R$. Clearly, if $\nu > 1/(\gamma - 1)$, then $\omega_{\rm BV}^2 > 0$ and convective stability is guaranteed. For $\gamma = 5/3$, this requires $\nu > 1.5$. The multiple requirements of a flat density profile, hydrostatic equilibrium and convective stability, as well as analytic simplicity, lead us to the following choice for the density profile of the envelope:

$$\rho(r) = \left(\frac{3}{2\pi}\right) \frac{(1 - r)^2}{r}. \tag{24}$$

The normalization is such that the total envelope mass $M_{\rm env} = 1$. The corresponding pressure and internal energy profiles can be easily determined by solving the hydrostatic equilibrium equation analytically. Figure 10 shows the mass profile of our simple red giant model. For comparison, we also show the mass profile obtained from a realistic stellar structure calculation (from Schwarzschild 1958, Table 28.7). Clearly, the agreement is excellent.

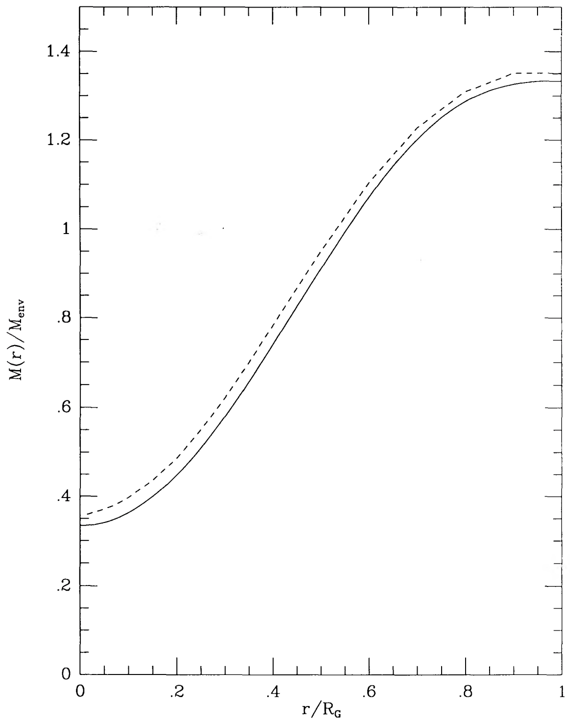

FIG. 10.—Mass profile of our simple red giant model (*solid line*). Note that mass here is in units of the total *envelope* mass $M_{\rm env}$. For comparison, the dashed line shows the mass profile for the realistic giant model of Schwarzschild (1958, Table 28.7). The small, nearly constant shift between the two curves is entirely due to the slightly larger core mass in the realistic model ($M_{\rm core}/M_G = 0.26$ instead of $M_{\rm core}/M_G = 0.25$ adopted in our case).

In the calculations of this section, the density profile of equation (24) is represented by varying the number density of a distribution of SPH particles with equal masses. There are now two point masses in the calculation: the compact object and the giant's core. Here we take $M_c = 7/3$ for the mass of the compact object, corresponding to the case of a 1.4 $M_\odot$ neutron star colliding with the 0.8 $M_\odot$ subgiant described above. Both point masses interact with the gas through a softened gravitational potential, as explained in § 3. The gravitational interaction between the two point masses themselves is calculated exactly, without softening.

4.2. *Numerical Results*

Consider the response of the giant envelope to its penetration by a point mass. For near-grazing collisions, the presence of the stellar core has little influence and the hydrodynamical behavior of the envelope is very similar to what we observed for a polytrope. The small binding energy of the giant envelope, however, allows gas to be extracted more easily and larger deformations of the envelope are generally observed for a given r_p. As the periastron distance decreases, we again observe a transition to a qualitatively different regime where the envelope is completely destroyed by the impact. The hydrodynamics of such an encounter is illustrated in Figure 11. Here the point mass was placed on a parabolic orbit with $r_p = 0.05$, one stellar radius above the stellar surface at $t = 0$. Note that a true head-on collision, with $r_p = 0$, is not possible here since the gravitational force between the two point masses would diverge. Conventions are as in Figure 6. Time is in units of $\tilde{t}$ (cf. eq. [23]). Up to periastron, at $t \approx 0.7$, a comparison with the corresponding encounter with a polytrope (Fig. 6) reveals no qualitatively new feature in the hydrodynamics. The moment when the core passes through the shock practically coincides with periastron. After periastron ($t = 0.8$ and $t = 1.0$), the core is quickly ejected from what remains of the star. However, its motion through the shocked gas remains very subsonic. In fact, throughout the calculation, the core appears to comove with the fluid without perturbing it much. Immediately after periastron, a large vortex forms around the perturber. No such vortex appears around the core, even though some gas will eventually remain bound to it (see below).

As was shown in Paper I, high-velocity, hyperbolic encounters can lead to core ejection on a much smaller time scale than envelope disruption (see also Tuchman 1985 and Livne & Tuchman 1988). This does not happen for parabolic encounters. Figure 12 shows how the core ejection takes place for the same collision as in Figure 11. Clearly, the time scales for core ejection and for the disruption of the envelope are comparable. Note that very little gas remains bound to the ejected core. This is a typical example of the "exchange mechanism" discussed in Paper I: the intruder point mass appears to have replaced the core inside the envelope.

The analysis of the various subsystems produced by the encounter is somewhat easier here than it was for polytropes. This is because there are always exactly three components in the final state of the system. Indeed, the star is never completely destroyed in the present case, since at the very least its core remains intact. In particular, for parabolic encounters, *a long-lived binary system is always formed.* Table 3 summarizes the properties of the various components, as well as the orbital parameters of the binary. The procedure used to determine these numbers was described in § 3. Notations are as in Table 1, except that here the subscript 2 identifies the gas that remains bound to the stellar core. The transition to "near–head-on" encounters is less abrupt than in the case

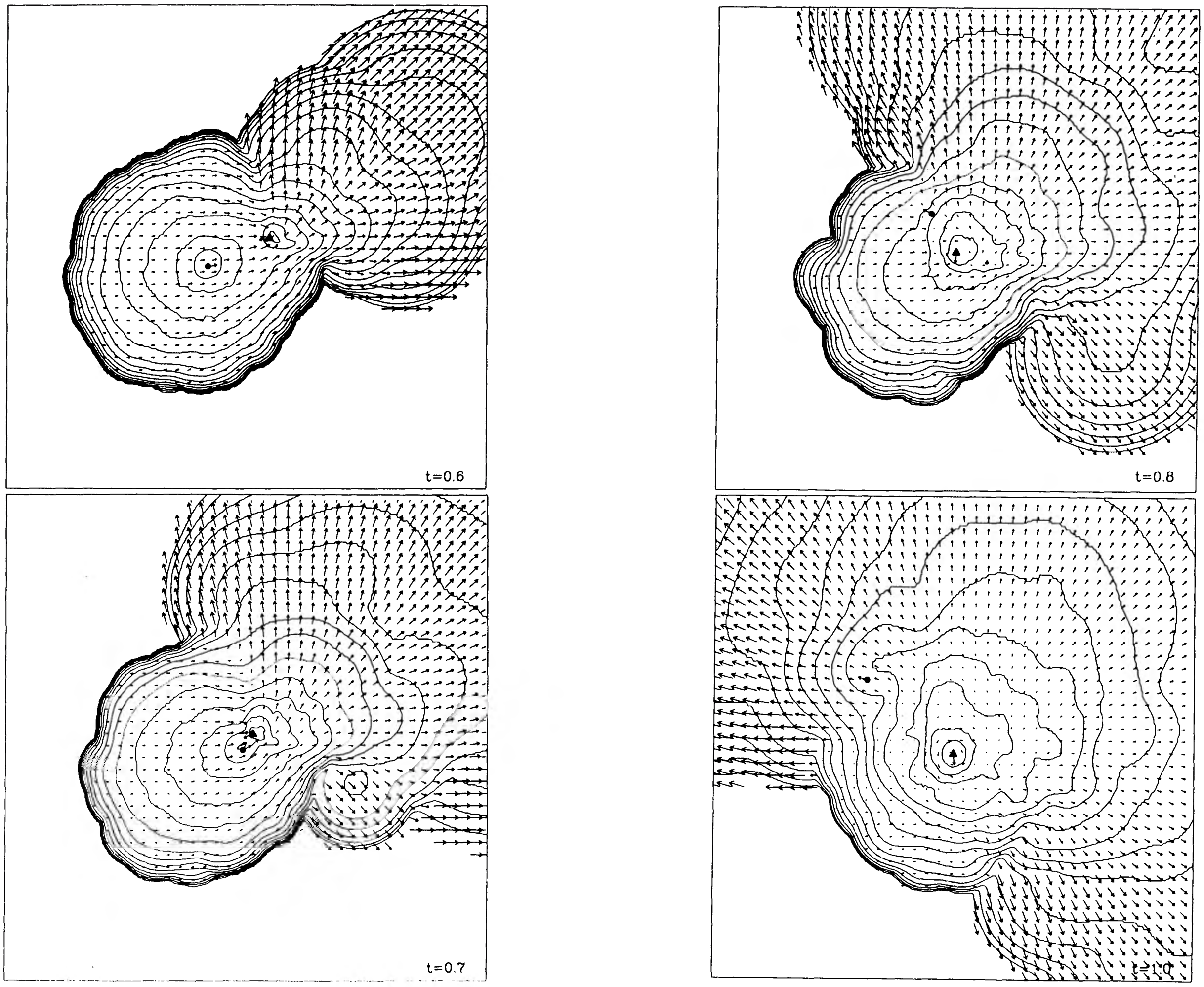

FIG. 11.—Density contours and velocity field in the orbital plane for a near head-on parabolic encounter between a compact object and a giant star. The solid triangle represents the compact object. The solid round dot represents the giant's core. Time is in units of $\tilde{t}$ (eq. [23]). At $t = 0$, the compact object was placed on a parabolic orbit, one stellar radius above the surface. The periastron separation of the initial (unperturbed) orbit was $r_p = 0.05$.

of a polytrope and occurs for a somewhat smaller value of the periastron distance, $r_p \approx 0.5$. In all encounters with $r_p < 0.5$, most of the gas remains bound to the neutron star, forming a massive disk, while the ejected core ends up practically bare. For encounters with $r_p > 0.5$ the envelope is not completely disrupted by the first interaction with the perturber but will be destroyed during subsequent interactions since the compact object keeps returning on bound orbits with smaller and smaller periastron distances. Moreover, the outer layers of the envelope keep expanding because of tidal deformation and induced rotation. *These nonlinear effects are still present for encounters with periastron separation as large as* $r_p \approx 2.5$. One might worry that for such distant encounters, the poor spatial resolution of the calculation in the outer region of the envelope could lead to large numerical errors. To check the validity of our results in this regime, we repeated the calculation of the $r_p = 2$ encounter, increasing the number of particles to $N = 4 \times 10^4$, and representing the envelope by a *uniform* distribution of particles with varying masses (cf. § 2.2). We found that the results were practically unchanged. For example, the mass captured by the compact object was $M_1 = 0.027$, in agreement with the 3% quoted in Table 3.

The orbital period of the binary has a minimum for some $0 < r_p < R_G$ along the sequence of parabolic encounters. This is because the ejection velocity of the core and the amount of energy transferred to its subsequent orbital motion increase rapidly as r_p approaches zero. We find that the minimum occurs for a collision with $r_p \approx 0.2$ (cf. Table 3). For such an encounter the orbit formed by the two components after the initial interaction has a period $P \approx 4$ (in units of $\tilde{t}$) which is small enough for us to be able to follow the subsequent orbital evolution of the system. We tracked a total of seven consecutive encounters for this case. Figure 13 shows particle plots at successive periastra and apastra. After each encounter, we redetermine the properties of all components using the procedure of § 3. The results of this calculation are presented in Table 4. Figure 14 shows the time evolution of the orbital energy and angular momentum. It is clear that after just a few orbits, no gas remains bound to the core. About half of the original envelope mass has been lost, while the remaining half now forms a massive disk ($M_1 \approx 0.3\ M_\odot$) around the neutron star. The periastron distance of the binary remains about an order of magnitude smaller than the equatorial radius of the disk. As a result, the persistent

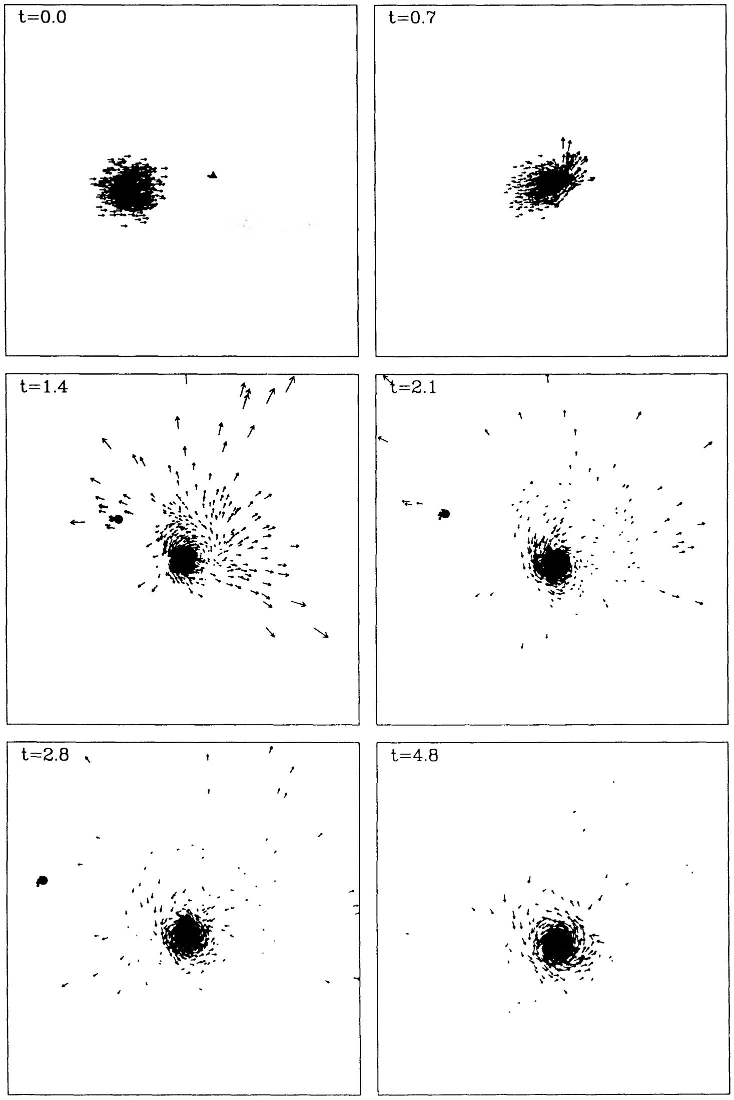

FIG. 12.—Sequence of particle plots in the orbital plane for the same encounter as in Fig. 11

drag force exerted on the core as it moves through the gas causes both the orbital period and the eccentricity of the binary to decay. Note that mass loss from the disk also persists at a steady and rather rapid rate: about 6% of the mass is removed after each passage. From the numbers in Table 4, we see that the time scale for mass loss is much smaller (by about an order of magnitude) than the time scale on which the orbital eccentricity decays. If the mass losses continue at the same rate for just about 10 more orbits, virtually no gas will be left in the binary system. In the absence of a dissipation mechanism, the orbital decay will stop (on a dynamical time scale). In this case the orbit could stabilize while still retaining a large eccentricity ($e \approx 0.7$ if it keeps decaying at a constant rate). This is exactly what we found in Paper I, where we were able to follow the orbital evolution much longer, until practically all gas particles had been ejected from the binary. Very near the compact object, of course, some small amount of gas is likely to remain. The thermal evolution of this gas is rather uncertain (see Krolik 1984 for a discussion). In particular, it is unclear whether the radiation pressure generated by the accretion of a small fraction of the gas might blow away the rest of the disk. Note, however, that even the accretion of a very small amount of gas ($\sim 10^{-2}\ M_\odot$) can be sufficient to spin-up a neutron star to millisecond periods (see, e.g., van den Heuvel, van Paradijs, & Taam 1986).

5. DISCUSSION

What are the implications of our results for binary formation in globular clusters? To answer this question, we must first know the critical periastron separation for tidal capture. This turns out to be much more difficult to calculate for giants than for polytropes. Indeed, in the tidal limit, the energy dissipation depends critically on a precise treatment of nonadiabatic processes (McMillan et al. 1987). Recently, McMillan et al. (1990) have performed PT calculations of tidal capture for realistic stellar models of a 0.8 $M_\odot$ star. For the capture of a 1.4 $M_\odot$ neutron star with a relative velocity at infinity of 10 km s^{-1}, they found that the critical

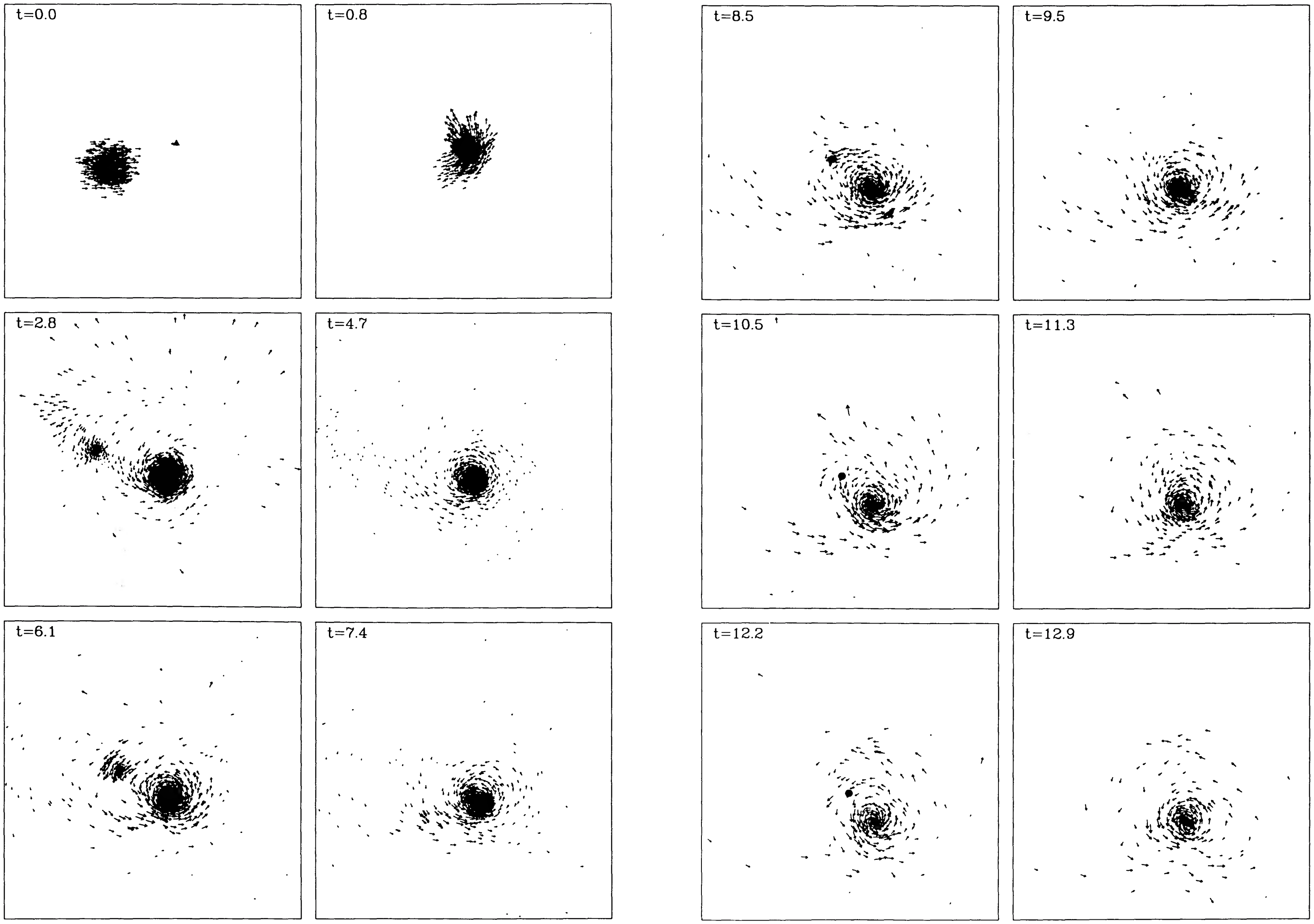

FIG. 13.—Particle plots showing the long-term evolution of the binary formed after a collision between a compact object and a giant star. The initial parabolic orbit has a periastron distance $r_p \approx 0.2$. The times shown correspond to successive apastra (*left*) and peristra (*right*).

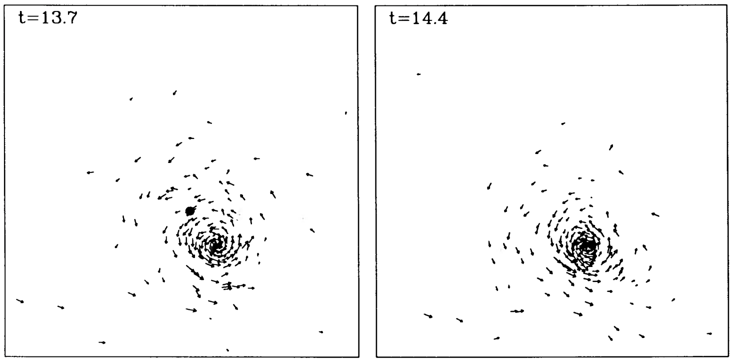

FIG. 13—*Continued*

separation for capture decreases as the star evolves, from $2.4R_G$ at the base of the subgiant branch to $1.45R_G$ at the onset of helium burning. This significant reduction from the typical value of $\approx 3R$ found for polytropes was also predicted by Bailyn (1988) on the basis of a simple argument. An important consequence of the results presented in Table 3 is that even for *distant encounters*, with periastron separations as large as $r_p \approx 2.5R_G$, *nonlinear tidal distorsions of the envelope, including mass transfer, are apparent.* Therefore, we must conclude, in agreement with Bailyn (1988), that *tidal capture of a neutron star by a giant in a globular cluster is likely to result in the destruction of the giant.*

The number of binary pulsars detected in globular clusters has increased dramatically over the past few months. Table 5 lists all presently known globular cluster binary sources, both low-mass X-ray binaries (LMXB) and binary radio pulsars, with a measured orbital period.

Several binary pulsars with long orbital periods ($P \gtrsim 1$ day) have recently been discovered. The standard formation scenario for these sources involves the tidal capture of a neutron star by a giant (Verbunt 1990; Romani 1990). Following the capture, the orbit is assumed to circularize, *with the giant star remaining undisturbed.* Normal stellar evolution would then lead to envelope expansion and Roche lobe overflow, forming an X-ray binary. When the giant envelope is exhausted, a recycled pulsar with a low mass degenerate companion would remain. Based on this scenario, McMillan et al. (1990) have calculated in detail the orbital evolution of the wide binary in M4. They concluded that the system could have been formed by the tidal capture of a neutron star by a

TABLE 3

NUMERICAL RESULTS FOR GIANT STAR[a]

	DISK				STAR				ORBIT		
r_p[b]	M_1	J_1	r_1	z_1	M_2	J_2	r_2	z_2	P_{orb}	e	r_p
0.05.........	0.68	0.19	1.0	0.8	0.003	0.0002	0.6	0.6	27.	0.98	0.05
0.20.........	0.62	0.50	1.4	0.7	0.06	0.004	0.1	0.1	3.7	0.86	0.16
0.50.........	0.32	0.46	2.5	1.0	0.50	0.07	0.4	0.3	6.8	0.85	0.24
1.0..........	0.10	0.11	1.7	0.6	0.84	0.12	0.6	0.4	38.	0.83	0.86
1.5..........	0.05	0.08	1.5	0.4	0.92	0.08	0.5	0.4	130.	0.88	1.4
2.0..........	0.03	0.05	1.8	0.4	0.96	0.06	0.5	0.4	440.	0.93	1.9
2.5..........	0.01	0.03	2.1	0.5	0.98	0.03	0.4	0.3	1600.	0.96	2.47

[a] Units are such that $G = M_{env} = R_G = 1$.

[b] Periastron separation of the unperturbed initial orbit.

TABLE 4

NUMERICAL RESULTS FOR THE ORBITAL EVOLUTION OF THE BINARY[a]

	DISK				STAR				ORBIT		
NUMBER	M_1	J_1	r_1	z_1	M_2	J_2	r_2	z_2	P_{orb}	e	r_p
0..........	0.0	...	...	...	1.0	0.0	0.3	0.3	...	1.0	0.2
1..........	0.62	0.50	1.4	0.7	0.06	0.004	0.1	0.1	3.7	0.86	0.16
2..........	0.63	0.54	1.9	1.1	0.02	0.0006	0.06	0.06	2.6	0.83	0.14
3..........	0.62	0.52	2.3	1.3	0.006	0.0002	0.05	0.05	2.0	0.81	0.13
4..........	0.59	0.48	2.5	1.5	0.0	...	...	...	1.6	0.80	0.12
5..........	0.56	0.46	2.7	1.7	0.0	...	...	...	1.5	0.79	0.12
6..........	0.53	0.44	2.9	1.9	0.0	...	...	...	1.4	0.78	0.12
7..........	0.49	0.40	3.0	2.0	0.0	...	...	...	1.3	0.77	0.12

[a] Units are such that $G = M_{env} = R_G = 1$.

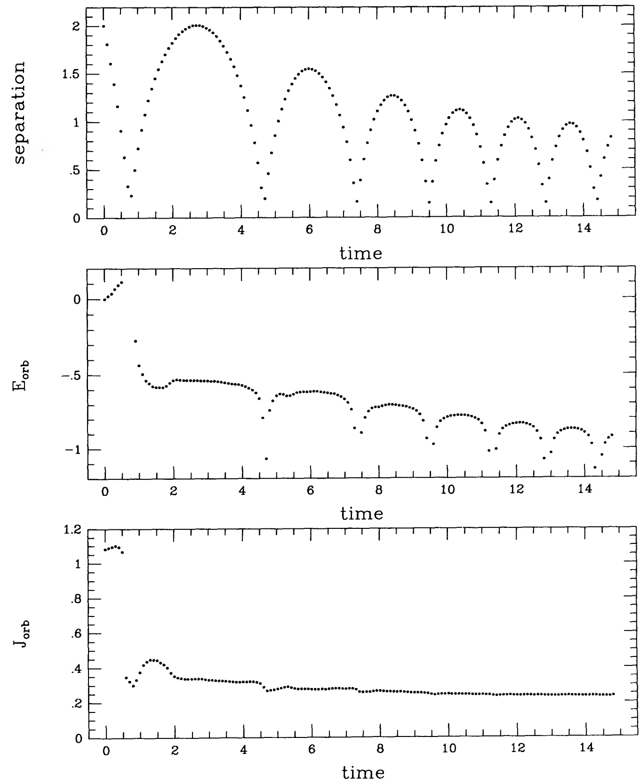

FIG. 14.—Long-term evolution of the system for the same $r_p = 0.2$ encounter shown in Fig. 13. Binary separation, orbital energy, and orbital angular momentum are shown as a function of time.

$R_G = 24\ R_\odot$ giant with $r_p/R = 1.7$–2. Clearly, our results indicate that this formation scenario is very unlikely, since the envelope of the giant would already be disrupted significantly after the first close passage of the neutron star. Apart from being in conflict with our theoretical calculations, the standard formation scenario also has problems explaining the observations. Romani (1990) has calculated the expected distribution of binary periods corresponding to this scenario and found it difficult to explain the large number of long period binaries.

Instead of the standard scenario involving tidal capture followed by circularization of the orbit and normal stellar evolution of the giant, our results suggest that cluster pulsars in wide, circular binaries may be formed as follows. A close encounter ($1 \lesssim r_p/R_G \lesssim 2$) takes place between a neutron star and a giant. After at most a few orbits, the envelope is completely destroyed. A stable (on a dynamical time scale) binary system results, consisting of a low-mass degenerate core in orbit around a neutron star surrounded by a massive disk. Eventually, on a much longer time scale, the orbit circularizes (at $a \sim R_G$) and an accretion disk forms, giving rise to a (possibly short-lived) LMXB–like phase. Finally, after the disk has been either exhausted or expelled, a spun-up pulsar in a wide,

TABLE 5

BINARY SOURCES IN GLOBULAR CLUSTERS

Source	Cluster	P_p (ms)	$f(M_\odot)$	P_{orb} (days)	e	References
X 2127+119	M15	−(LMXB)	?	0.35	?	1
4U 1820−303	NGC 6624	−(LMXB	?	0.008	?	1
PSR 1620−26	M4	11.1	0.007	191	0.025	2
PSR 2127+11C	M15	30.5	0.145	0.34	0.674	3
PSR 1516+02B	M5	7.95	?	6.9	>0.1	4
PSR 1310+18	M53	33.2	0.0098	256	<0.01	5,6
PSR 1744−24A	Terzan 5	11.6	0.00032	0.075	Small	7
PSR 1802−075	NGC 6539	23.1	0.0097	2.62	0.22	8
PSR 0021−72E	47 Tuc	3.54	?	≈2	?	9
PSR 0021−72H	47 Tuc	3.21	?	?(long)	?	9
PSR 0021−72I	47 Tuc	3.49	?	?(long)	?	9
PSR 0021−72J	47 Tuc	2.10	?	0.12	?	9
PSR 0021−72K	47 Tuc	1.79	?	?	?	9

REFERENCES—(1) Parmar & White 1988; (2) Lyne et al. 1988; (3) Anderson et al. 1990b, (4) Wolszczan et al. 1989; (5) Anderson et al. 1989; (6) Kulkarni et al. 1991; (7) Lyne et al. 1990; (8) D'Amico et al. 1990; (9) Lyne 1991.

circular binary remains. Note that if most of gas in the massive disk around the neutron star is lost rapidly enough after the initial encounter, the binary may retain a large eccentricity (cf. § 4), as observed in the NGC 6539 and M5 binaries. Calculations by Rappaport, Putney, & Verbunt (1989) indicate that such a large eccentricity is unlikely to have been induced by three-body encounters, given the very moderate central concentration of these clusters (cf. Chernoff & Djorgovski 1989). Alternatively, formation scenarios involving primordial binaries (which are now believed to exist in significant numbers in globular clusters; cf. Pryor 1990) have been proposed, which could explain the presence of wide-orbit binary pulsars even in very sparse clusters, such as M53 (see Kulkarni et al. 1991).

For the ultrashort period systems, such as the 11 minute binary in NGC 6624, the standard formation scenario involves a *collision* between a neutron star and a giant (Verbunt 1987, 1990). Following the collision it is assumed that the orbit circularizes *inside* the envelope and that subsequent "slow spiral-in" can lead to a very short binary period. This scenario also appears to be in conflict with our results, which show that the envelope is disrupted well before circularization occurs, let alone any secular spiral-in. However, our calculations assumed a mass ratio characteristic of conditions in globular cluster *today*. Slow spiral-in of a neutron star inside the envelope of a giant might be possible when the giant is much more massive ($M_G/M_c \gtrsim 10$) than the neutron star (Taam, Bodenheimer, & Ostriker 1978). If the age of the binary system is comparable to the age of the cluster (as in the model proposed by Rappaport et al. 1987 for the 11 minute binary), then it is possible that the formation may have taken place at an early epoch in the history of the cluster, when the masses of giants could still have been $\gg 1\ M_\odot$. However, the lifetime of such massive giants may be too short for any collision to occur at all. Moreover, hydrodynamical calculations by Bodenheimer & Taam (1984) of the response of the envelope to the deposition of frictional energy during spiral-in indicate that even for very massive giants ($M_G/M_c = 16$ in their study), ejection of the envelope probably occurs well before an ultrashort binary period is reached. Our results suggest that the collision of neutron star with a more massive giant might lead to a system where the degenerate core orbits the neutron star inside a massive disk. After circularization of the orbit, however, the degenerate core and the disk are corotating, and it is not clear whether a spiral-in can occur.

For binaries with orbital periods of a few hours, such as 47 Tuc J, the standard formation scenario involves the tidal capture of a neutron star by a *main-sequence* star (Verbunt 1990; Bailyn & Grindlay 1987). Following the capture, the orbit would quickly circularize, and then decay by loss of angular momentum. The main-sequence star is assumed to remain unperturbed throughout the orbital evolution, until the onset of mass transfer. Note that systems with orbital periods of a few hours could also be formed by a collision between a neutron star and a subgiant. Indeed, the calculations of § 4 indicate that the size of the orbit can be as small as $\sim 0.1 R_G$ (see also Paper I). For a subgiant of radius $R_G \approx 10\ R_\odot$ this implies a binary separation $a \sim 1\ R_\odot$ and an orbital period $P \lesssim 1$ day. While our own dynamical calculations do not rule out the standard formation scenario for these short-period binaries (cf. § 3), a recent study by Ray et al. (1987) of the long-term effects of tidal energy dissipation in main-sequence stars indicate that here also, the star could be disrupted well before mass transfer begins. Moreover, if all tidal captures of neutron stars by main-sequence stars were to result in the formation of short-period binary pulsars, a large cluster population of such objects would be expected. These could have remained undetected in pulse searches, given the large Doppler smearing in short-period binaries. Sensitive images of five globular clusters made recently with the VLA by Kulkarni et al. (1990a) revealed that such a population does not exist, leading these authors to conclude that the tidal capture of a neutron star by a main-sequence star must indeed lead to the complete disruption of the main-sequence star and the formation of an *isolated* millisecond pulsar.

It is clear from our discussion that the standard formation scenario for globular cluster pulsars may need substantial revision. In particular, it appears that accretion from a massive disk, rather than accretion from a stellar companion, could be the prevalent mechanism for the formation of spun-up pulsars. The duration of the accretion phase in this case is the lifetime of the disk, which could be much shorter than the corresponding LMXB lifetime in the standard scenario. Indeed, studies of the population of cluster pulsars indicate that the birthrate of these objects may exceed that of LMXBs by a factor $\gtrsim 100$ (Kulkarni, Narayan, & Romani 1990). Moreover, a shorter accretion phase could also explain why many cluster pulsars have rather long pulse periods (of the 28 cluster pulsars presently known, 11 have a pulse period > 10 ms; cf. Lyne 1991). Detailed physical studies of the thermal evolution of massive disks around neutron stars appear highly desirable at this point.

Close encounters may also be of considerable importance for the evolution of the globular clusters themselves. Indeed, if, as suggested above, all tidal captures and collisions (with main-sequence stars as well as giants) lead to the disruption of the star, then the total rate of mass loss from globular cluster cores may be much higher than previously estimated, possibly providing an efficient mechanism for halting core collapse (see, e.g., Goodman & Hut 1989). Clearly, a reexamination of this problem also seems desirable at this point.

We thank C. Bailyn, M. Davies, L. Hernquist, M. Ruffert, and F. Verbunt for making useful comments on the manuscript. This work was supported by NSF grant AST 90-15451 and by NASA grant NAGW-666. Computations were performed on the Cornell National Supercomputer Facility, a resource of the Center for Theory and Simulation in Science and Engineering at Cornell University, which receives major funding from the National Science Foundation and IBM corporation, with additional support from New York State and members of its Corporate Research Institute.

REFERENCES

Aarseth, S. J. 1985, in Multiple Time Scales, ed. J. U. Brackbill & B. I. Cohen (Orlando: Academic), 377

Allen, M. P., & Tildesley, D. J. 1989, Computer Simulation of Liquids (New York: Oxford Univ. Press)

Anderson, S., Kulkarni, S., Prince, T., & Wolszczan, A. 1989, IAU Circ., No. 4853

———. 1990a, IAU Circ., No. 5013

Anderson, S. B., Gorham, P. W., Kulkarni, S. R., Prince, T. A., & Wolszczan, A. 1990b, Nature, 346, 42

Bailyn, C. D. 1988, Nature, 332, 330

Bailyn, C. D., & Grindlay, J. E. 1987, ApJ, 316, L25

Benz, W., & Hills, J. G. 1987, ApJ, 323, 614

Benz, W., Hills, J. G., & Thielemann, F. K. 1989, ApJ, 342, 986

Bodenheimer, P., & Taam, R. E. 1984, ApJ, 280, 771

Chernoff, D. F., & Djorgovski, S. 1989, ApJ, 339, 904

Courant, R., & Friedrichs, K. O. 1976, Supersonic Flow and Shock Waves (New York: Springer)

Cox, J. P. 1980, Theory of Stellar Pulsation (Princeton: Princeton Univ. Press)

D'Amico, N., et al. 1990, IAU Circ., No. 5013

Evans, C. R., & Kochanek, C. S. 1989, ApJ, 346, L13

Evrard, A. E. 1988, MNRAS, 235, 911

Fabian, A. C., Pringle, J. E., & Rees, M. J. 1975, MNRAS, 172, 15P

Fryxell, B. A., Taam, R. E., & McMillan, S. L. W. 1987, ApJ, 315, 536

Giersz, M. 1986, Acta Astr., 36, 181

Gingold, R. A., & Monaghan, J. J. 1977, MNRAS, 181, 375

Goodman, J., & Hut, P. 1989, Nature, 339, 40

Hernquist, L. 1987, ApJS, 64, 715

Hernquist, L., & Katz, N. 1989, ApJS, 70, 419

Hockney, R. W., & Eastwood, J. W. 1988, Computer Simulations Using Particles (Bristol: Adam Hilger)

Joss, P. C., Rappaport, S., & Lewis, W. 1987, ApJ, 319, 180

Krolik, J. H. 1984, ApJ, 282, 452

Kulkarni, S. R., Anderson, S. B., Prince, T. A., & Wolszczan, A. 1991, Nature, in press

Kulkarni, S. R., Goss, W. M., Wolszczan, A., & Middleditch, J. 1990a, ApJ, 363, L5

Kulkarni, S. R., Narayan, R., & Romani, R. W. 1990b, ApJ, 356, 174

Lattanzio, J. C., Monaghan, J. J., Pongracic, H., & Schwarz, M. P. 1985, MNRAS, 215, 125

Lee, H. M., & Ostriker, J. P. 1986, ApJ, 310, 176

Livne, E., & Tuchman, Y. 1988, ApJ, 332, 271

Lucy, L. B. 1977, AJ, 82, 1013

Lyne, A. G. 1991, in Proc. of NATO Advanced Research Workshop on X-ray Binaries and the Formation of Binary and Millisecond Radio Pulsars, ed. E. P. J. van den Heuvel, in press

Lyne, A. G., Biggs, J. D., Brinklow, A., Ashworth, M., & McKenna, J. 1988, Nature, 332, 45

Lyne, A. G., et al. 1990, Nature, 347, 650

McMillan, S. L. W., McDermott, P. N., & Taam, R. E. 1987, ApJ, 318, 261

McMillan, S. L. W., Taam, R. E., & McDermott, P. N. 1990, ApJ, 354, 190

Monaghan, J. J. 1985, Comp. Phys. Rep., 3, 71

———. 1989, J. Comp. Phys., 82, 1

Monaghan, J. J., & Lattanzio, J. C. 1985, A&A, 149, 135

Nagasawa, M., Nakamura, T., & Miyama, S. M. 1988, PASJ, 40, 691

Parmar, A. N., & White, N. E. 1988, in X-ray Astronomy with *EXOSAT*, ed. R. Pallavicini & N. E. White (Firenze: Memorie della Società Astronomica Italiana), 43

Press, W. H., & Teukolsky, S. A. 1977, ApJ, 213, 183 (PT)

Pryor, C. 1990, BAAS, 22, 1308

Rappaport, S., Nelson, L. A., Ma, C. P., & Joss, P. C. 1987, ApJ, 322, 842

Rappaport, S., Putney, A., & Verbunt, F. 1989, ApJ, 345, 210

Rasio, F. A., & Shapiro, S. L. 1990, ApJ, 354, 201 (Paper I)

———. 1991, in preparation

Ray, A., Kembhavi, A. K., & Antia, H. M. 1987, A&A, 184, 164

Romani, R. W. 1990, ApJ, 357, 493

Romani, R. W., Kulkarni, S. R., & Blandford, R. D. 1987, Nature, 329, 309

Różyczka, M., Yorke, H. W., Bodenheimer, P., Müller, E., & Hashimoto, M. 1989, A&A, 208, 69

Ruffert, M., & Müller, E. 1990, A&A, 238, 116 (RM)

Schwarzschild, M. 1958, Structure and Evolution of the Stars (New York: Dover)

Shapiro, P. R., Kang, H., & Villumsen, J. V. 1989, in Workshop on Large-Scale Structures and Peculiar Motions in the Universe, ed. D. W. Latham & L. N. da Costa (ASP Conf. Ser.), in press

Shima, E., Matsuda, T., & Inagushi, T. 1986, MNRAS, 221, 687

Sod, G. A. 1978, J. Comp. Phys., 27, 1

Sutantyo, W. 1975, A&A, 44, 227

Taam, R. E., Bodenheimer, P., & Ostriker, J. P. 1978, ApJ, 222, 269

Tuchman, Y. 1985, ApJ, 288, 248

Tuchman, Y., Sack, N., & Barkat, Z. 1978, ApJ, 219, 183

van den Heuvel, E. P. J., van Paradijs, J. A., & Taam, R. E. 1986, Nature, 322, 153

Verbunt, F. 1987, ApJ, 312, L23

———. 1990, in Neutron Stars and Their Birth Events ed. W. Kundt (Dordrecht: Kluwer), 179

Verbunt, F., & Meylan, G. 1988, A&A, 203, 297

Wells, N. H., Burrus, C. S., Desobry, G. E., & Boyer, A. L. 1990, Comp. Phys., 4, 507

Wolszczan, A., Anderson, S., Kulkarni, S., & Prince, T. 1989, IAU Circ., No. 4880